N-62862

DESIGN AND TESTS OF A SIX-STAGE AXIAL-FLOW COMPRESSOR HAVING A TIP SPEED OF 550 FEET PER SECOND AND A FLAT OPERATING CHARACTERISTIC AT CONSTANT SPEED

By

John W. Maynard, Jr.

Thesis submitted to the Graduate Faculty of the Virginia Polytechnic Institute in candidacy for the degree of MASTER OF SCIENCE in Aeronautical Engineering

APR 1971 RECEIVED NASA STI FACILITY INPUT BRANCH

N71 72514 (ACCESSION NUMBER) 73 (PAGES) TMX-67040 (NASA CR OR TMX OR AD NUMBER) (THRU) None (CODE) (CATEGORY) FACILITY FORM 602

April 1958

DESIGN AND TESTS OF A SIX-STAGE AXIAL-FLOW COMPRESSOR HAVING A TIP SPEED OF 550 FEET PER SECOND AND A FLAT OPERATING CHARACTERISTIC AT CONSTANT SPEED

By John W. Maynard, Jr.

ABSTRACT

A six-stage axial-flow compressor with a 550 feet per second tip speed and a flat operating characteristic (constant stagnation-pressure ratio at constant speed over the operating range of the compressor) was designed and tested. The design theory and test results are presented in this thesis. It was designed for a constant power input per pound of flow regardless of mass flow. The design specific weight flow was 21.1 pounds per second per square foot of frontal area with an atmospheric discharge at an overall stagnation-pressure ratio of 3.25 and an inlet hub-tip radius ratio of 0.7. In order to reach design conditions the blade setting angles were reset and the machining notches at the root of the first three rotor blades were filled. In an attempt to increase the flat operating range of the compressor, the blade setting angles of the first two stages were increased and those of the last two stages were decreased. Also, the solidity of the first rotor was decreased.

DESIGN AND TESTS OF A SIX-STAGE AXIAL-FLOW COMPRESSOR HAVING A TIP SPEED OF 550 FEET PER SECOND AND A FLAT OPERATING CHARACTERISTIC AT CONSTANT SPEED

by

John W. Maynard, Jr.

Thesis submitted to the Graduate Faculty of the
Virginia Polytechnic Institute
in candidacy for the degree of
MASTER OF SCIENCE
in
Aeronautical Engineering

APPROVED:

Director of Graduate Studies

Dean of Engineering

APPROVED:

Head of Department

Major Professor

April 1958

Blacksburg, Virginia

TABLE OF CONTENTS

		PAGE
I.	LIST OF FIGURES AND TABLES	3
II.	INTRODUCTION	7
III.	SYMBOLS	12
IV.	DESIGN	14
	General Vector Diagram Consideration	14
	Vector Diagram Selection	16
	Blade Selection	21
	Mechanical Design	24
V.	EXPERIMENTAL TESTS	26
	Apparatus	26
	Instrumentation and Test Procedure	27
	Presentation of Results	32
VI.	DISCUSSION OF RESULTS	36
VII.	CONCLUSIONS	44
VIII.	ACKNOWLEDGMENTS	45
IX.	BIBLIOGRAPHY	46
X.	VITA	47
XI.	APPENDICES	48
	Appendix A. Derivation of an Equation for the Rate of Change of Work Input With a Change in Axial Velocity	48
	Appendix B. Effect of Testing With Freon-12	49

I. LIST OF FIGURES AND TABLES

FIGURE		PAGE
1.	General Vector Diagram	53
2.	Typical Constant Speed Overall Performance for Three Types of Axial-Flow Compressors	54
3.	Typical Symmetrical Vector Diagram	55
4.	Design Vector Diagram for First Stage of Six-Stage Compressor at Several Radii	56
5.	Six-Stage Compressor Assembly Configuration A	57
	(a) Rotor Assembly	57
	(b) Stator Assembly	58
6.	Detail of Blade Mounting and Notches in Blade	59
7.	Sectional View of Compressor	60
8.	Plan View of the Compressor Test Stand	61
9.	Instruments	62
10.	Six-Stage Compressor Assembly After Solidity Change, Configuration B	63
	(a) Rotor Assembly	63
	(b) Stator Assembly	64
11.	Stagnation Pressure and Temperature Distribution Against Radius for Design Speed	65
12.	Overall Performance of a Six-Stage Axial-Flow Compressor Configuration A in Air	66
	(a) Variation of Stagnation-Pressure Ratio (Numerical Average) With Percent of Design Mass Flow	66

FIGURE PAGE

12. (Continued)

(b) Variation of Temperature Efficiency (Numerical Average) With Percent of Design Mass Flow 67

(c) Variation of Tip Static-Pressure Rise With Blade Row 68, 69

13. Overall Performance of a Six-Stage Axial-Flow Compressor Configuration B in Air 70

(a) Variation of Stagnation-Pressure Ratio (Numerical Average) With Percent of Design Mass Flow 70

(b) Variation of Temperature Efficiency (Numerical Average) With Percent of Design Mass Flow 71

(c) Variation of Tip Static-Pressure Rise With Blade Row at 100-Percent Design Speed 72

14. Overall Performance of a Six-Stage Axial-Flow Compressor Configuration C in Air 73

(a) Variation of Stagnation-Pressure Ratio (Numerical Average) With Percent of Design Mass Flow 73

(b) Variation of Temperature Efficiency (Numerical Average) With Percent of Design Mass Flow 74

(c) Variation of Tip Static-Pressure Rise With Blade Row at 100-Percent Design Mass Flow 75

15. Overall Performance of a Six-Stage Axial-Flow Compressor Configuration C in Freon-12 76

(a) Variation of Stagnation-Pressure Ratio (Numerical Average) With Percent of Design Mass Flow 76

FIGURE PAGE

15. (Continued)

(b) Variation of Temperature Efficiency (Numerical Average) With Percent of Design Mass Flow 77

(c) Variation of Tip Static-Pressure Rise With Blade Row 78, 79

16. Overall Performance of a Six-Stage Axial-Flow Compressor Configuration D in Air 80

(a) Variation of Stagnation-Pressure Ratio (Numerical Average) With Percent of Design Mass Flow 80

(b) Variation of Temperature Efficiency (Numerical Average) With Percent of Design Mass Flow 81

(c) Variation of Tip Static-Pressure Rise With Blade Row at 100-Percent Design Speed 82

17. Overall Performance at a Six-Stage Axial-Flow Compressor Configuration D in Freon-12 83

(a) Variation of Stagnation-Pressure Ratio (Numerical Average) With Percent of Design Mass Flow 83

(b) Variation of Temperature Efficiency (Numerical Average) With Percent of Design Mass Flow 84

(c) Variation of Tip Static-Pressure Rise With Blade Row at 100-Percent Design Speed 85

18. Overall Performance of a Six-Stage Axial-Flow Compressor Configuration E in Air 86

(a) Variation of Stagnation-Pressure Ratio (Numerical Average) With Percent of Design Mass Flow 86

FIGURE PAGE

18. (Continued)

(b) Variation of Torque Efficiency With Percent of Design Mass Flow 87

(c) Variation of Tip Static-Pressure Rise With Blade Row at 100-Percent Design Speed 88

19. Overall Performance of a Six-Stage Axial-Flow Compressor Configuration E in Freon-12 89

(a) Variation of Stagnation-Pressure Ratio (Numerical Average) With Percent of Design Mass Flow 89

(b) Variation of Temperature Efficiency (Numerical Average) With Percent of Design Mass Flow 90

(c) Variation of Tip Static-Pressure Rise With Blade Row at 100-Percent Design Speed 91

TABLE

I. Design Values for Test Compressor 19

II. Blade Designations 23

III. Summary of Configurations Tested 33

IV. Summary of Test Data 35

II. INTRODUCTION

For the design of supersonic aircraft and engine-in-wing plan forms, the engine with the smallest frontal area is desired. In the past, the compressors used in turbojet engines were centrifugal type compressors. Since the largest component of a turbojet engine (using a centrifugal compressor) is the compressor assembly, then to decrease the frontal area of a turbojet engine only the compressor frontal area need be reduced. Because of their smaller cross section and capability of high mass flows, axial-flow compressors have been developed for turbojet engine use. At the present time, axial-flow compressors can be designed for a smaller diameter than the combustion chamber while delivering the required mass flow. In comparison to centrifugal compressors, axial-flow compressors can deliver a greater weight flow per square foot of frontal area at a slightly greater efficiency, in the order of 7-percent (ref. 1). The design of an axial-flow compressor is simplified since the compressor can be studied stage by stage or investigated as a complete unit. Most of the work being conducted at the present time is on axial-flow compressors.

The design tip speed of an axial-flow compressor is usually selected as high as possible within the limitation imposed by the drag rise Mach number relative to the rotor blades. This high tip speed is desired since the pressure rise per stage increases exponentially with the tip speed for the same blades and the same flow angles. As a result of considerable research and development effort, the tip speed and pressure ratio of aircraft gas-turbine type compressors have been greatly increased in recent years.

Low tip speed compressors have some advantages such as structural design, airfoil selection, and lower relative air velocities, if the pressure ratio per stage can be maintained at a moderately high level. The lower tip speed design has application to industrial-type compressors and to the rear stages of aircraft jet-engine compressors. The rear stages of an aircraft jet-engine compressor operate at low corrected (temperature) tip speeds. To illustrate this consider a two spool compressor, (each spool independently driven on a common axis), at a flight Mach number of 2.5 in the stratosphere. Assume that the first spool has an overall stagnation-pressure ratio of 2.0 and the tangential tip speed in the second spool is 1,000 feet per second. For these conditions the second spool will have a corrected tip speed of 675 feet per second. In order to operate a compressor at low tip speeds, higher turning angles are required to keep the work-input high enough to obtain the desired stagnation-pressure ratio at a reasonable operating efficiency. Impulse-type blades produce these desired high turning angles and a reasonable stagnation-pressure ratio at good operating efficiencies.

Two parameters used in the design of compressor blades are the stagnation pressure rise coefficient $\left(\frac{\Delta P}{P_{1,R} - p_{1,R}}\right)$ and the static pressure rise coefficient $\left(\frac{\Delta p}{P_{1,R} - p_{1,R}}\right)$. It has been found from cascade data (ref. 4) that the static-pressure rise coefficient is significant loading-limit parameter for compressor blades. The entering relative impact pressure is mainly a function of the rotational speed and the axial velocity. The design and performance of a low speed

impulse-type rotor with and without a stator row is presented in references 2 and 3. In this design a very high stagnation pressure rise coefficient was attained with reasonable temperature efficiencies and the values of the static-pressure rise coefficient were within allowable limits. Since the entering relative impact pressures were low, the static-pressure rise in the rotor was approximately zero. This left a large static-pressure rise for the stator and resulted in a high velocity leaving the stator. Therefore, this rotor design was not suitable for multistaging, because of this large velocity increase.

It is possible to increase or decrease the entering relative impact pressure of the rotor by using guide vanes (prerotational blades) if the rotational speed and the work done by the rotor is held constant. For a multistage compressor where axial flow is desired at all radii for all stages, guide vanes are of no particular advantage. The present trend in aircraft axial-flow compressor design is to increase the entering relative impact pressure to higher values by designing for supersonic (relative) inlet velocities. The high relative velocities are attained by raising both the axial velocity and the rotational speed. The objective of the present work was to obtain information on combining low rotational speeds and moderetely high axial velocities. In doing so, the relative Mach number entering the rotor will be in the high subsonic range; this will produce relative impact pressures which are high enough to permit stagnation pressure ratios in the order of 1.2 per stage with symmetrical victor diagrams for all stages that have no increase in axial velocities across each stage. This type of rotor is suitable for multistaging.

If the compressor is to be driven by a constant speed electric motor it would be desirable to have a wide operating range of mass flow rates occurring at a constant stagnation-pressure ratio and at a constant speed. In the case of an aircraft compressor this condition would also be desirable. For illustration, consider a two spool compressor. If the first spool was designed for the condition that there be a constant stagnation-pressure ratio over the operating range of mass flow at constant speed then the vector diagrams for the second spool would be less critical.

A six-stage compressor was designed for the following: (1) symmetrical velocity vector diagrams (to be explained in the design section); (2) constant axial velocity of 650 feet per second at all stages; (3) a 550 feet per second tip speed; (4) stagnation-pressure ratio of 1.217 per stage, 3.25 overall; (5) inlet hub-tip radius ratio of 0.7; (6) specific weight flow of 21.3 pounds per second per square foot of frontal area; and (7) a flat operating characteristic (constant stagnation-pressure ratio at constant speed over the operating range of the compressor). The compressor was built and tested as described in this thesis. The design had a possible immediate application to a boundary-layer suction control for a large slotted throat transonic wind tunnel, but would be equally applicable to other installations where a low tip-speed compressor is advantageous. For the boundary-layer suction control, the compressor was to be driven by a constant-speed electric motor, therefore, a flat operating characteristic was required. In the

expectation of achieving a flat operating characteristic the compressor was designed for constant power input per pound of flow.

Any multistage compressor that is designed for air, and has symmetrical vector diagrams at all stages, can be run in other mediums without serious mismatch (that is, the design vector diagrams not being obtained at all radii and all stages). Since Freon-12 has a higher density than air, it will produce a higher weight flow at a given angle of attack without increasing stall. To illustrate this condition, the compressor was tested in both air and Freon-12.

To the knowledge of the author this is the first compressor designed for the foregoing conditions. The design, testing, and analysis of results was conducted at the Cascade Aerodynamics Laboratory of the Langley Aeronautical Laboratory.

The design theory of this compressor will be taken up in Section IV.

III. SYMBOLS

B	number of blades
C_{l_o}	camber expressed as isolated airfoil lift coefficient, perpendicular to mean velocity
c_p	specific heat at constant pressure, $\frac{\text{ft-lb}}{\text{slug } ^\circ\text{R}}$
EMS	equivalent tip speed, ft/sec
M	Mach number
m	mass, $\frac{\text{lb sec}}{\text{ft}}$
n	number of degrees of freedom
P	total pressure, lb/sq ft
p	static pressure, lb/sq ft
R1, R2, . . .	rotor 1, rotor 2, etc.
r	radius, ft
S1, S2, . . .	stator 1, stator 2, etc.
T	stagnation temperature, $^\circ$R
U	rotation speed, ft/sec
V	velocity of medium, ft/sec
α	angle between entering flow direction and blade chord, deg
α_{LSC}	angle between entering flow direction and blade chord for optimum conditions from low-speed cascade data, deg
α_{req}	angle between entering flow direction and blade chord required to match previous stage, deg
β	flow angle measured from axial direction, deg

γ ratio of specific heats

η_p polytropic efficiency

η_Q efficiency based on torque, $\eta_Q = \dfrac{mc_p T_1 \left[\left(\frac{P_2}{P_1}\right)^{\frac{\gamma-1}{\gamma}} - 1.0\right]}{\omega(\text{Torque})_{\text{measured}}}$

η_T efficiency based on temperature, $\eta_T = \dfrac{\left[\left(\frac{P_2}{P_1}\right)^{\frac{\gamma-1}{\gamma}} - 1.0\right] T_1}{(T_2 - T_1)}$

θ flow turning angle, deg

ρ density, slug/cu ft

σ solidity, chord/spacing ratio

ω angular velocity, radians/sec

Subscripts:

1 entering rotor

2 leaving rotor

3 leaving stator

4 leaving stator no. 6

h hub

R relative to rotor

S stator

t tip

z axial

θ tangential

The use of commas in the subscripts denotes the second subscript refers to the symbol but not the first subscript.

IV. DESIGN

General Vector Diagram Considerations

In order to understand the vector diagrams presented for the design of this compressor, a brief description of a typical vector diagram (shown in Fig. 1) is given. For the general case a flow with prerotation has been assumed. The entering flow velocity is V_1 with a prerotation of β_1 degrees. This flow velocity, V_1, can be broken down into its axial and tangential components, $V_{z,1}$ and $V_{\theta,1}$ respectively. Subtracting the rotational velocity, U, from the entering tangential velocity, $V_{\theta,1}$, and adding vectorially to this the axial velocity, $V_{z,1}$, results in the entering velocity relative to the rotor, $V_{1,R}$, at a direction of $\beta_{1,R}$ degrees. Now assume the flow is turned θ_R degrees by the rotor. The flow velocity leaving the rotor has a magnitude of $V_{2,R}$ at an angle of $\beta_{2,R}$ degrees in rotor coordinates, where $\beta_{2,R} = \beta_{1,R} - \theta_R$. This flow velocity, $V_{2,R}$, can be broken down into its axial and tangential components, $V_{z,2}$ and $V_{\theta,2,R}$, respectively. To convert this back to the stationary coordinate system, the rotational velocity U is added to the leaving tangential velocity in rotor coordinates, $V_{\theta,2,R}$, and this result is added vectorially to the axial velocity behind the rotor $V_{z,2}$. The resultant flow velocity, V_2, denotes the flow leaving the rotor in stationary coordinates in a direction of β_2 degrees. If it is assumed now that the flow is turned θ_S degrees by the stator, then the flow velocity leaving the stator is V_3 in a direction of β_3 degrees, where $\beta_3 = \beta_2 - \theta_S$. Again this flow velocity

V_3 can be broken down into its axial and tangential components, $V_{z,3}$ and $V_{\theta,3}$, respectively. A composite diagram, which is most commonly used, is shown in Figure 1.

For the design of the compressor in this thesis, the velocity diagrams were selected to produce a flat operating characteristic (constant stagnation pressure ratio over the operating range of mass flow) at constant rotational speed or, more specifically, to have a constant power input per pound of flow at a constant rotational independent of the axial velocity. The following equation expresses the rate of change of the work input per unit mass flow with respect to a change in the axial velocity and is derived in Appendix A:

$$\frac{\dfrac{d\left(\Delta V_\theta\right)}{\Delta V_\theta}}{\dfrac{dV_z}{V_z}} = 1.0 - \frac{U}{\Delta V_\theta}$$

The following assumptions were made in the derivation:

1. Entering and leaving axial velocities are equal.
2. Streamlines remain at the same radii.
3. Leaving flow direction relative to the rotor remains constant as the entering direction β_1 varies.

Conventional axial-flow compressors have a rotational speed (U) two or three times as great as the change in tangential velocity across the rotor (ΔV_θ) and hence their constant speed operating line has a high negative slope as shown in Figure 2. The impulse compressor of

references 2 and 3 has a rotational speed less than the change in the tangential velocity at some of the blade-setting angles tested and thus had a positive sloping operating line as shown in Figure 2. For a positive sloping operating line the stagnation pressure rise will increase with increasing weight flow over the operating range of the compressor. For a flat operating characteristic, or zero slope line, the change in tangential velocity must equal the rotational speed. (See Fig. 2).

Vector Diagram Selection

Since a flat operating characteristic was desired for this compressor, it was necessary to make the change in tangential velocity across the rotor equal to the rotational speed. This can only be done at one radius if the power input is to be constant along the span of the blades. For this design the power input was assumed constant radially and the mean radius was selected to have the change in tangential velocity equal to the rotational speed. From experience a hub-tip radius ratio of 0.7 was selected for the first rotor. Several factors which guided this selection were that the compressor weight and inlet corss section were not critical and it was believed that such a high hub-tip radius ratio would produce the flat operating characteristic desired. It was assumed that the flow direction was axial at all radial stations. On the assumption that axial flow existed at all stages and that the power input would be constant over the span of the blade for all stages, no guide vanes were used. With no guide vanes, both the rotor and the stator could be designed to turn the flow axially, in their respective coordinates,

only at the mean radius for all stages. Therefore, the vector diagrams are symmetrical only at the mean radius. A typical symmetrical vector diagram is shown in Figure 3. Note that here the axial velocity is equal in magnitude to the rotational velocity.

The numerical values of the rotational speed, and hence, the stagnation-pressure ratio per stage, were selected by considering the blade diffusion limits and the Mach number attainable without choking. The diffusion limit used was the static-pressure rise divided by the relative entering impact pressure, $\frac{\Delta p}{P_{1,R} - p_{1,R}}$. A maximum value of 0.5 was selected from cascade data for this parameter. The relative entering impact pressure was made as high as practical to attain a high pressure ratio per stage. Hence, the only limit on the relative entering impact pressure is that of choking in the blade passage. The inlet-air angles are low and the solidities are high so as to produce the high turning angles required. With these high solidities and low inlet-air angles the entering Mach number is limited to about 0.77 at the mean radius. Increasing the axial velocity or the rotational speed was considered equally effective as a means of attaining a high relative impact pressure. In other words, the limiting value of the diffusion limit was considered to be independent of the rotor inlet-air angle.

After selecting the overall design values such as; stagnation pressure ratio, weight flow, inlet hub-tip radius ratio, and the condition that the axial velocity shall be constant at all radial stations, a two dimensional design was computed. To simplify the computing, the

density was assumed constant at all radii. Since constant density along the radii was used to find the approximate values, only the mean radius was computed. After several trials, the number of stages required to produce the given overall stagnation pressure ratio without exceeding stage limitations was determined. Also, the rotational speed, the magnitude of the axial volocity, and the hub-tip radius ratio for all stages was fixed. Using the results of this computation a three-dimensional free-vortex design was computed. For this design the density was assumed a variable along the blade span. Considering the first stage and the conditions that the power input is constant along the span, the density is a variable, and that simple radial equilibrium exists downstream of the blade, the weight flow was checked using the values from the previous two-dimensional design. If the conditions could not be met, the only variable that has not been fixed is the hub-tip radius ratio. When all the conditions were met the next stage was computed. Since there were numerous iterations to be done, this work was carried out on a Bell Analog computer. From the three dimensional design vector diagrams, trial blade selections were made to check the choking Mach number. This complete method was carried through several times before the final design was selected. For the final design an axial velocity of 650 feet per second and a tip speed of 550 feet per second were chosen. The average stagnation pressure ratio per stage was set at 1.217 which permitted an overall design pressure ratio of 3.25 to be attained in six stages. The vector diagrams for the first stage are shown in Figure 4 and pertinent numerical values for all stages are given in Table I (see page 19).

TABLE I.- DESIGN VALUES FOR TEST COMPRESSOR

Blade row	Radius	M	V_z, ft/sec	V_θ, ft/sec	β, deg	θ, deg	σ	Chord	c_{l_o}	α, deg	$\beta - \alpha$, deg	$\alpha - \alpha_{LSC}$, deg	$\alpha - \alpha_{req}$, deg
R1	0.667	0.786	650	550.7	40.3	28.9	1.30	2.178	1.40	18.1	22.2	2.1	0
	.582	.746		481.0	36.5	36.5	1.42	2.089	1.70	21.6	14.9	2.1	0
	.498	.710		411.3	32.3	45.4	1.60	2.000	2.00	25.4	6.9	2.1	0
S1	.667	.689	650	420.1	32.9	32.9	1.40	2.345	1.61	18.4	14.5	0	0
	.582	.720		481.0	36.5	36.5	1.48	2.172	1.78	20.5	16.0	0	0
	.498	.765		562.5	40.9	40.9	1.60	2.000	1.98	23.2	17.7	0	0
R2	.667	.759	650	550.7	40.3	30.5	1.28	2.140	1.52	18.6	21.7	1.4	-.5
	.595	.726		491.3	37.1	37.1	1.38	2.064	1.78	21.7	15.4	1.9	0
	.523	.695		431.9	33.6	44.6	1.51	1.988	2.04	25.1	8.5	2.0	-.8
S2	.667	.674	650	438.3	34.0	34.0	1.40	2.345	1.61	19.5	14.5	1.1	-.1
	.595	.701		491.3	37.1	37.1	1.47	2.198	1.73	21.3	15.8	1.3	-.2
	.523	.737		558.8	40.7	40.7	1.56	2.051	1.91	23.4	17.3	1.2	0
R3	.667	.733	650	550.7	40.3	31.8	1.35	2.116	1.60	18.8	21.5	1.6	.8
	.605	.705		499.6	37.6	37.6	1.44	2.051	1.83	21.6	16.0	1.8	.8
	.543	.679		448.6	34.6	44.0	1.55	1.983	2.05	24.5	10.1	1.4	1.0
S3	.667	.659	650	453.3	34.9	34.9	1.40	2.345	1.61	20.4	14.5	2.0	-.4
	.605	.682		499.6	37.6	37.6	1.46	2.219	1.72	22.0	15.6	2.0	-.4
	.543	.712		556.5	40.6	40.6	1.53	2.092	1.86	23.8	16.8	2.2	0
R4	.667	.709	650	550.7	40.3	32.8	1.34	1.007	1.59	20.0	20.3	2.1	0
	.613	.685		506.4	37.9	37.9	1.46	1.007	1.75	22.2	15.7	2.1	0
	.560	.663		462.2	35.4	43.5	1.60	1.007	1.91	24.6	10.8	2.1	0
S4	.667	.644	650	465.7	35.6	35.6	1.34	1.023	1.83	19.9	15.7	0	0
	.613	.664		506.4	37.9	37.9	1.46	1.023	1.88	21.3	16.6	0	0
	.560	.688		554.9	40.5	40.5	1.60	1.023	1.93	22.7	17.8	0	0
R5	.667	.686	650	550.7	40.3	33.7	1.34	1.007	1.63	20.6	19.7	2.3	0
	.620	.666		512.0	38.2	38.2	1.44	1.007	1.77	22.6	15.6	2.4	0
	.573	.648		473.3	36.1	43.1	1.56	1.007	1.91	24.8	11.3	2.5	-.3
S5	.667	.629	650	476.0	36.2	36.2	1.34	1.023	1.83	20.5	15.7	.6	.1
	.620	.646		512.0	38.2	38.2	1.44	1.023	1.87	21.7	16.5	.5	-.2
	.573	.667		553.8	40.4	40.4	1.56	1.023	1.92	22.9	17.5	.6	-.1
R6	.667	.665	650	550.7	40.3	34.5	1.34	1.007	1.66	21.4	18.9	2.9	.5
	.626	.648		516.6	38.5	38.5	1.43	1.007	1.79	23.2	15.3	2.9	-.2
	.584	.632		482.6	36.6	42.8	1.53	1.007	1.91	25.1	11.5	3.1	0
S6	.667	.615	650	484.7	36.7	36.7	1.34	1.023	1.83	21.0	15.7	1.1	-.1
	.626	.629		516.6	38.5	38.5	1.43	1.023	1.87	22.1	16.4	1.1	-.1
	.584	.647		553.1	40.4	40.4	1.53	1.023	1.91	23.2	17.2	1.3	0

The throat area for the first rotor was within 5 percent of the two-dimensional choking value at all radial stations for design flow. No allowance was made for boundary layer displacement thickness in the inlet and none for the boundary-layer growth through the compressor except as included in the design adiabatic efficiency assumption. The adiabatic efficiency $\left(\eta_{adiabatic} = \frac{T_1\left[\left(\frac{P_2}{P_1}\right)^{\frac{\gamma}{\gamma-1}} - 1.0\right]}{\Delta T_{measured}}\right)$ is the ideal temperature rise based on isentropic conditions divided by the actual or measured temperature rise. In order to obtain a realistic value of the actual temperature rise in the design of a compressor, the stagnation pressure ratio exponent (in the isentropic temperature rise expression) is multiplied by an efficiency value which includes losses from boundary-layer growth, boundary-layer displacement in the inlet, differences between real gas values and perfect gas values, irregularities in the flow, . . . etc. This efficiency is given the name of polytropic efficiency. The design efficiency then becomes

$$\eta_{adiabatic} = \frac{T_1\left[\left(\frac{P_2}{P_1}\right)^{\frac{\gamma}{\gamma-1}} - 1.0\right]}{T_2\left[\left(\frac{P_2}{P_1}\right)^{\frac{\eta p \gamma}{\gamma-1}} - 1.0\right]}$$

For most conventional compressor designs a value of 90-percent polytropic efficiency has been found by experience to be reliable. A value of

85-percent polytropic efficiency was believed realistic for this compressor considering that the wakes of one blade row have a considerably lower velocity relative to the following row which is not the case of more conventional higher tip-speed compressors. In the conventional compressor, the velocity in the wake relative to the following row is approximately equal in magnitude to that of the free-stream air. These velocities have a large gradient in flow angle compared with that of the free stream inlet flow. In this design, the wakes have a smaller difference in direction and a larger deficit in velocity. This low-energy air is able to continue flowing downstream through the diffuser, that is, the next blade row, because it receives energy from the free stream by turbulent mixing. This mixing was arbitrarily assumed to result in a 5-percent penalty in polytropic efficiency. The exact value of 85.8-percent polytropic efficiency was chosen because the polytropic exponent of the temperature is then a convenient integer for use in the Bell Analog computer. The design adiabatic efficiency, or temperature efficiency, for the design stagnation pressure ratio of 3.25 was found to be 82.8 percent.

Blade Selection

An NACA $a = 1.0$ (uniform loading on isolated airfoils) meanline with an NACA 16-series thickness distribution was used for all blades. These were selected because the resulting flow passage (between blades) had a streamwise variation of cross-sectional area that was considered desirable. The reason being that the minimum area (or throat) occurred

between the 5-percent and 20-percent chord points, and the passage area increased smoothly from that point to the trailing edge. Another important consideration dictating this choice was the large amount of cascade data available for this meanline.

A maximum thickness of 8-percent was selected for all blade sections. This was a compromise between the desire for thin blade sections (from choking considerations) and for thick blade sections (to permit a wide angle-of-attack range and to provide a thick enough rotor blade root section so that a threaded shank fastening could be used).

The blade section cambers and setting angles were found directly from the low-speed cascade data of reference 5. The designation of the blade sections selected in given in Table II, (see page 23). There are only four different blade types in the compressor, these are for rotors and stators 1, 2, and 3, and rotors and stators 4, 5, and 6. Each row within the group differs only in radial length and blade setting angle. The blades were selected for the vector diagrams of the first row of each group. The blades were then matched as well as possible to the next two rows. For rotor number 3 it was necessary to change the solidity in order to meet the design vector diagrams. In Table I (see page 19), the column labeled $\alpha - \alpha_{lsc}$ is the amount the design angle of attack differs from the angle of attack selected for a peak-free pressure distribution at low speed as published in reference 5. The column labeled $\alpha - \alpha_{req'd}$ shows the difference between the angle of attack at which the blade would produce the desired turning angle and the angle

TABLE II

BLADE DESIGNATIONS

Blade row	Radius (ft)	Blade designation	Blade row	Radius (ft)	Blade designation
	0.667	$16(14A_{10})08$		0.667	$16(15.9A_{10})08$
R1	.582	$16(17A_{10})08$	R4	.613	$16(17.5A_{10})08$
	.498	$16(20A_{10})08$		.560	$16(19.1A_{10})08$
	.667	$16(16.1A_{10})08$		.667	$16(18.3A_{10})08$
S1	.582	$16(17.8A_{10})08$	S4	.613	$16(18.8A_{10})08$
	.498	$16(19.8A_{10})08$		.560	$16(19.3A_{10})08$
	0.667	$16(15.2A_{10})08$		0.667	$16(16.3A_{10})08$
R2	.595	$16(17.8A_{10})08$	R5	.620	$16(17.7A_{10})08$
	.523	$16(20.4A_{10})08$		.573	$16(19.1A_{10})08$
	.667	$16(16.1A_{10})08$		.667	$16(18.3A_{10})08$
S2	.595	$16(17.3A_{10})08$	S5	.620	$16(18.7A_{10})08$
	.523	$16(19.1A_{10})08$		.573	$16(19.2A_{10})08$
	0.667	$16(16A_{10})08$		0.663	$16(16.6A_{10})08$
R3	.605	$16(18.3A_{10})08$	R6	.626	$16(17.9A_{10})08$
	.543	$16(20.5A_{10})08$		.584	$16(19.1A_{10})08$
	.667	$16(16.1A_{10})08$		.667	$16(18.3A_{10})08$
S3	.605	$16(17.2A_{10})08$	S6	.626	$16(18.7A_{10})08$
	.543	$16(18.6A_{10})08$		.584	$16(19.1A_{10})08$

of attack that is available using the first blade of each group. The available angle of attack is a function of the blade twist and the requirements of the other radial stations of the same blade.

All the blade chords for the first three stages were made about 2 inches in length so that the Reynolds number could be kept above one-quarter million for an atmospheric discharge pressure at design conditions. The chord of the blades for the last three stages was approximately 1.0 inch.

Mechanical Design

The complete six-stage axial-flow compressor, as tested at design blade setting angles, is shown in Figures 5(a) and 5(b). The blades for the first three stages were fabricated from 20(24)T aluminum alloy, while those for the last three stages were fabricated from 416 heat-treated stainless steel. All blades were cut on an airfoil duplicating machine and hand polished. The blades were mounted by turned shanks which allowed variable blade setting angles. To finish turn the shanks, notches were cut in the blade roots as shown in Figure 6. Because of the contour of the inner case, the shank size, and the chord length, the notches were largest in rotors 1, 2, and 3. These notches extended over 6 percent, 7 percent, and 8 percent of the blade span, respectively.

With the high solidities chosen, there would be no clearance between the blade fastening nuts when a simple drilled drum was used. The stresses would have exceeded a safe margin when the compressor was operated at 20-percent overspeed in air if the shell had been thin enough to permit the use of a simple drilled drum. For these reasons a slotted drum,

with individual mounting blocks, as shown in Figure 6, was used. Figure 6 also shows the method used to hold the last block in place. Using this type of fastening allowed the solidity to be changed in any of the rotors by removing blades and inserting spacing blocks. The stator blades were mounted by drilling the outer casing.

Figure 7 is a cross section of the compressor. The diffuser was a 5.8° conical inner case (the diameter varying from 14 inches to 12 inches as shown in Figure 7) and a radial diffuser (shown in Figure 8). A roller bearing was installed on the inlet end of the shaft to carry the radial load and any transverse movement of the shaft caused by expansion. This bearing was lubricated by an oil-mist spray. The bearing assembly at the exist of the compressor consister of a roller bearing carrying the radial load and a Kingsbury type spherical seated thrust bearing carrying the thrust load. The rear assembly was lubricated by a pressurized liquid oil system.

From experience the tip clearance was set at from 0.023 to 0.025 inch when cold. This assured a reasonable allowance for expansion while running.

After the construction of the compressor was completed it was assembled in the test stand described in the next section.

V. EXPERIMENTAL TESTS

Apparatus

The compressor test stand was designed in accordance with NACA standards as described in reference 6, a plan view of which is shown in Figure 8. In order to have low turbulence uniform flow in the test section the following were used: (1) a 1-1/2 by 1-1/2 by 7 inch honeycomb grid; (2) three 100 mesh screens; (3) a 1-1/2 by 1-1/2 by 8 inch honeycomb grid; (4) a 60 mesh screen; and (5) a 20 to 1 reduction from a circular settling chamber to the annular test section (see Fig. 8). Located behind the test compressor is a vainless radial diffuser into which the test medium is discharged. This low velocity medium is then passed through two aircraft-type radiators which are used to remove the heat from the medium. A drum-type throttle valve, with a butterfly vane on the upstream end, is used to increase the back pressure on the compressor. This throttle valve consists of two concentric perforated drums, the outer one being driven by an electric actuator. When the holes in the two drums are about 50 percent closed, the butterfly vane is geared to close. This allows a sensitive control on the mass flow. Between the throttle valve and the settling chamber is a calibrated venturi. To assure low turbulent flow in the venturi, a 1-1/2 by 1-1/2 by 7-inch honeycomb grid was used in the inlet of the venturi.

With this installation the compressor can be tested in a medium of air or Freon-12 and also tested as a closed or open cycle system. To run as a closed cycle system the venturi is connected to the settling

chamber as shown by the dashed line in Figure 8. For the open cycle system tests (solid lines in Fig. 8), the air is filtered before entering the settling chamber. Between the filter and the settling chamber is a 20-inch diameter gate valve used for throttling. It is assumed that with the straightening vanes uniform flow is present at the inlet of the compressor for both systems. The air is discharged after passing through the venturi tube. For this compressor the temperature rise in air was larger than the temperature drop across the radiator, therefore, the open cycle system was used for all of the air testing. All testing in Freon-12 was done in a closed loop system. Since the contamination of the gas would produce erroneous results. The compressor was driven by a 3,000-horsepower induction motor with a two shaft, 2.015:1, Folk speed increase.

Instrumentation and Test Procedure

One method of indicating the overall performance of a compressor is by measuring the temperature efficiency and the mass flow. The temperature efficiency can be computed from the overall stagnation temperature rise and the overall stagnation pressure rise (see temperature efficiency equation in symbols). The mass flow is measured by the calibrated venturi meter (Fig. 8). Another efficiency used is the torque efficiency which is computed from the work done on the medium and the torque required to do this work (see torque efficiency equation in symbols). These are both overall values. The static pressure rise along the outer case gives an indication how each blade row is performing in relation to the others.

For this compressor radial rakes were used to measure the stagnation temperature and the stagnation pressure (Fig. 9). The approximate location of the measuring stations are: Station 1, 3 inches ahead of the first rotor; station 2, 1 inch behind the sixth stator; and station 3, 6.5 inches behind the sixth stator as shown in Figure 7.

The inlet stagnation temperature distribution was measured by five double-shielded chromel-alumel thermocouples equally spaced, 0.16 inches apart, along a radial rake (Fig. 9). The rake was equally spaced in the annulus at station 1. The inlet stagnation pressure was measured by two 0.015-inch diameter static-pressure orifices in the settling chamber. From previous calibrations, it was found that these static-pressure orifices indicated the same pressure as a stagnation pressure probe in the inlet. The absolute inlet stagnation temperature was indicated by two double-shielded iron-constantan thermocouple bells in the settling chamber. The radial static pressure distribution was checked around the outer case at station 1 by four, 0.015-inch diameter, static-pressure orifices equally spaced around the circumference.

The exit instrumentation for the first three tests was located at station 3. Two stagnation temperature rakes of the same type as used at station 1 were used to measure the stagnation temperature at station 3. The stagnation pressure distribution was measured by two stagnation pressure rakes (Fig. 9) consisting of eleven 0.060-inch diameter tubes each. Each of these rakes, stagnation temperature and stagnation pressure, were equally spaced radially across the annulus. The two stagnation

temperature rakes were located at 0° and 180° around the circumference looking in the direction of flow and the two stagnation pressure rakes were located at 90° and 270° around the circumference looking in the same direction. The static-pressure distribution was checked around the outer case at stations 2 and 3 by four equally spaced 0.015-inch diameter static-pressure orifices located at each station.

For the remaining tests, one of the stagnation temperature rakes and one of the stagnation pressure rakes were moved from station 3 to station 2. This was done to determine whether there was any change in the radial distribution closer to the sixth stator. The circumferential location of the stagnation temperature and stagnation pressure rakes at stations 2 and 3 was determined so that the rakes were in the center of one of the sixth stator blade passages. It was assumed that the wakes from the sixth stator had little effect on the resulting measurements.

The compressor equivalent weight flow (weight flow based on standard conditions of pressure and temperature) was determined from the calibrated venturi meter (Fig. 8). All of the stagnation temperatures were indicated on a recording Minneapolis Honeywell self-balancing potentiometer. All of the stagnation and static pressures were indicated on a multiple-tube back-lighted mercury manometer board and recorded simultaneously by photographing the manometer board. The rotor speed was measured by a commercial Strobocon tuning instrument. A fluctuation of 1 percent was found to be present in the control system.

In order to obtain an indication of the work done by each blade row static-pressure orifices, 0.015-inch in diameter, were located

ahead of each blade row in the same position relative to the blades as shown in Figure 10(b).

The velocity of sound in Freon-12 air mixture was measured by an instrument similar to that described in reference 7. With this, the characteristics of the mixture and the physical properties of the the medium were determined.

In order to determine the effect on the compressor of moisture content in the test medium water was sprayed into the inlet. Four nozzles, equally spaced, and 22 inches ahead of the first rotor were used. The water was sprayed in at varying rates with the supply pressure (60 pounds per square inch) being the maximum. The amount of water injected was measured by a commercial flowmeter.

The following procedure was used when testing in air. In order to obtain a constant speed operating line the speeds were corrected to standard NACA temperature before running. This eliminated variations caused by variable inlet temperatures. A given corrected speed was set at full-open throttle. For these tests the upstream throttle was used. The stagnation temperature rise and shaft torque were recorded and a photograph was taken of the manometer board. At the same speed the throttle was closed in arbitrary increments, about 8 to 10, until the stall region was reached. The stall region was determined by the change in the stagnation pressure rise and the sound of the compressor. From past experience, it is known that compressors have a definite pulsating sound and vibration when the stall region is reached.

Vibration indicators were mounted at both the inlet and exit of the compressor on the outer casing to indicate these vibrations. From the vibration indicators, the pressure rise, and the audible sounds, the stall region was determined. For speeds of 70 percent of design and higher this point was the surge point, or point where the complete compressor had stalled and there was flow reversal. At lower speeds, it was the boundary of rotating stall. When data had been taken at all throttle position, the rotational speed was changed and the same procedure was followed.

The testing procedure was the same for operating in Freon-12 as that indicated above. The air speeds were corrected to Freon-12 speeds by the following relation, (ref. 8) assuming the same entering Mach number for air and Freon-12 testing.

$$\frac{ETS_{air}}{ETS_{Freon\text{-}12}} = \frac{\left[\dfrac{\gamma R}{2 + (\gamma - 1)M_1^2}\right]^{1/2}_{air}}{\left[\dfrac{\gamma R}{2 + (\gamma - 1)M_1^2}\right]^{1/2}_{Freon\text{-}12}}$$

The R in the above equation is the universal gas constant. Since a closed-loop system was used for operation in Freon-12 the system pressure could be controlled. It was set at about one-half an atmosphere for all Freon-12 tests. The throttle in the test stand was used for all the Freon-12 tests. The actual running procedure was the same as given for air.

The design configuration was designated as configuration A. In order to reach design conditions the blade setting angles were reset and the machining notches at the root of the blades in the first three rotors were filled. These modifications were designated as configurations B and C respectively. In an attempt to increase the flat operating range of the compressor the blade setting angles of the first two stages were increased and those of the last two stages were decreased. This modification was designated as configuration D. The solidity of the first rotor was decreased in an attempt to increase the flat operating range of the compressor. This modification was designated as configuration E.

Table III (see page 33) lists the configurations giving the geometric change, the speeds tested, and the test medium.

Presentation of Results

A typical radial distribution of the stagnation pressure ratio and the nondimensional stagnation temperature rise for the compressor discharge at design speed is shown in Figure 11.

The area weighted value of the stagnation pressure ratio can be found by first multiplying the stagnation pressure ratio by the incremental area that it acts on, summing these results over the annulus, and dividing by the annulus area, $\dfrac{\int_{r_h}^{r_t} \frac{P_4}{P_1}\, r\,dr}{\int_{r_h}^{r_t} r\,dr}$. It was found that the

TABLE III.- SUMMARY OF CONFIGURATIONS TESTED

Configuration	Description	Test medium	Speeds tested, (percent of design)
A	Original blade-setting angle, (see Table I p. 20)	Air	40, 50, 60, 75, 80, 85, 95, 100, 105
B	Blade-setting angles changed to raise angle of attack by R1 2° R3 0° R5 0° S1 4° S3 5° S5 5° R2 0° R4 0° R6 0° S2 5° S4 0° S6 0°	Air	60, 75, 80, 85, 95, 100, 105, 110
C	Same configuration as B except notches in R1, R2, and R3 were filled with balsa.	Air Freon-12	40, 60, 75, 80, 85, 95, 100 50, 60, 80, 85, 90, 95, 100, 105, 110, 115
D	Blade-setting angles changed to raise angle of attack by the following as compared to configuration A R1 5° R3 0° R5 -2° S1 4° S3 5° S5 5° R2 2° R4 0° R6 -2° S2 5° S4 0° S6 0°	Air Freon-12	60, 75, 80, 85, 95, 100, 105 60, 75, 85, 95, 100, 105
E	Same blade-setting angles as configuration D. Five blades removed from the first rotor.	Air Freon-12	30, 40, 50, 60, 75, 80, 85, 95, 100, 105, 110 30, 40, 50, 60, 75, 80, 85, 90, 95, 100, 105, 110

numerical average of the stagnation pressure ratio $\left(\frac{P_4}{P_1} = \sum_{n=1}^{n} \frac{1}{n} \frac{P_4}{P_1}\right)$

n = point number

approximately equal to the area weighted value when the end points of the numerical average were omitted. For reporting purposes, the numerical averages were used for both the stagnation pressure ratio and the stagnation temperature rise.

The overall performance of the several configurations tested is presented in Figures 12 through 19. A brief summary of the results appears in Table IV (see page 35).

A discussion of the results will follow in the next section.

TABLE IV

SUMMARY OF TEST DATA

Configuration	Figure number	Medium	Peak efficiency		Percent of mass flow at 100-percent design speed		
			85-percent design speed	100-percent design speed	Maximum flow	P_4/P_i 3.0	P_4/P_i 3.2
A	12	Air	80.0	83.0	96.0	88.0	-----
B	13	Air	79.5	77.5	100.0	100.0	-----
C	14	Air	82.0	82.5	101.5	101.5	101.5
C	15	Freon-12	81.0	81.0	105.0	104.5	104.0
D	16	Air	81.0	82.5	102.5	102.5	102.0
D	17	Freon-12	82.5	80.0	108.0	107.5	107.0
E	18	Air	*77.0	*77.0	102.0	102.0	102.0
E	19	Freon-12	80.5	82.0	106.0	106.0	105.5

*For this configuration the efficiency was based on torque measurements.

VI. DISCUSSION OF RESULTS

The compressor in its design configuration, configuration A, had the flat operating characteristic (constant stagnation pressure ratio at constant speed over the operating range of the compressor)(Fig. 12(a)) that it was designed for. It was low in mass flow by about 4 percent and had a peak stagnation pressure ratio of 3.0 as compared to the design value of 3.25. The temperature efficiency (Fig. 12(b)) at design speed was 83 percent compared with the design temperature efficiency of 82.8 percent. The power input to the compressor was low by about 32 percent of the design value. This indicates that the design turning angle was not attained in one or more of the blade rows. To obtain an indication of the rows that were not operating at design values without extensive surveys, the static pressure rise along the outer case was plotted (Fig. 12(c)). In all the rows except the fourth stator row the static pressure rise was below the design value. The points used are referenced to the stagnation pressure ratio map (Fig. 12(a)) by Roman numerals. At the high mass flows, or open throttle, the sixth stator was choked. For this configuration the static pressure distribution was presented for off design speeds (Fig. 12(c)). At off design speeds the compressor operated with the same characteristic as at design speed. The sixth stator choked at high mass flows and the overall shape of the static pressure distribution was the same. The flat operating characteristic is limited by the supersonic flow in the sixth stator at the high mass flows and the surge point or rotating stall region at

the other extreme. Since the compressor was below the design point the following changes were made. The first rotor and the first, second, third, and fifth stator blade rows were reset to higher blade setting angles as listed in Table III, (see page 33). This was done to increase the overall stagnation pressure ratio and the mass flow, and to more evenly distribute the static pressure distribution by increasing the work done by the blade rows that were below the design static pressure rise. The blade rows and the change in blade setting angles for these rows was determined from previous experience and the static pressure distribution.

In configuration B, the above changes were incorporated. This configuration reached the design mass flow (Fig. 13(a)), but at a pressure ratio of 3.1. The temperature efficiency (Fig. 13(b)) was 7 percent lower than the temperature efficiency found in configuration A (Fig. 12(b)). By increasing the blade setting angles in several of the blade rows the static pressure distribution was increased and more evenly distributed (Fig. 13(c)) as compared with that found in configuration A (Fig. 12(c)) at design speed. The sixth stator row choked at the high mass flows.

The notches (Fig. 6) at the root end of the blades of the first three rotors were believed to be partly responsible for the lower-than-design stagnation pressure ratio and temperature efficiency. These notches extended radially for 6 percent, 7 percent, and 8 percent of the blade span for rotors 1, 2, and 3, respectively. They could cause flow separation. If flow separation occurred it would cause a low stagnation pressure ratio and a low power input for this machine. These

notches were filled with balsa wood for the next configuration, configuration C, to ascertain whether separation was occurring and to attempt to correct this adverse effect.

The performance of configuration C is shown in Figure 14. Filling the notches raised the mass flow by 1-1/2 percent, the peak temperature efficiency by 6 percent, and the peak stagnation pressure ratio from 3.1 to 3.22, at design speed. The overall static pressure rise for configuration C (Fig. 14(c)) was increased to approximately the design distribution in all stages. By filling the notches and resetting the blade angles for several rows, the stagnation pressure ratio, the mass flow, and the static pressure rise were all raised to approximately design values at the same overall temperature efficiency (82 percent).

Configuration C was also tested using Freon-12 gas as a test medium. Because of the lower ratio of specific heats, the temperature rise in Freon-12 is less than that in air for the same stagnation pressure ratio. This results in a greater density rise in Freon-12. Appendix B shows that for this compressor, the density rise is effectively 24 percent greater in Freon-12 that in air. Because of this higher density, the compressor will pass more weight flow and will have a greater effective annulus area at the exit. With the higher wieght flow and lower sonic velocity, the blade rows will operate at higher angles of attack, progressively increasing from the inlet to the exit. This will cause stall at these higher weight flows and limit the operating range of the compressor.

Figure 15 shows the performance of configuration C tested in a Freon-12 medium. The peak temperature efficiency and peak stagnation pressure ratio are approximately the same as that found from testing this configuration C in air (Fig. 14), but the mass flow increased approximately 5 percent. At design speed, and above, the compressor had a smaller flat operating line for Freon-12 (Fig. 15(a)) as compared with the air tests (Fig. 14(a)). A possible reason for this was given in the foregoing paragraph. The static pressure rise at design speed and near stall (Fig. 15(c)) was approximately the same as for the air tests, but at the open throttle condition it was considerably lower in the mid-compressor stages. The higher mass flows and mismatch could account for this drop in static pressure rise. The dip in the static pressure rise only occurred at as low as 85 percent of design speed for off design operation. The sixth stator passage was choked at the high mass flows at design and off design speeds. After tests of configuration C were completed the exit instrumentation was changed to one stagnation temperature rake and one stagnation pressure rake (at station 2) and one of each instrument at station 3. The data used in the remaining configurations were taken from the instrumentation at station 2.

In an attempt to increase the weight flow operating range of the compressor, the blade setting angles of rotors 1, 2, 3, 5, and 6 were reset (as listed in Table III, see page 33) so as to increase the power input in the first two stages and decrease it in the rear stages. This modification will be noted as configuration D. Configuration D was

tested in air first and its performance map is shown in Figure 16. In comparison with configuration C tests with air (Fig. 14(a)) there was no change in the flat operating range and there was very little effect on the performance. As has been noted in previous configurations the sixth stator passage choked at all speeds for maximum flow conditions. At the maximum flow condition for all speeds the flow behind the sixth stator was supersonic. At some speeds, the instrumentation at station 2 indicated no change in stagnation pressure ratio at the maximum flow condition possibly due to this supersonic flow.

Configuration D was also tested with a Freon-12 medium. The overall performance is presented in Figure 17. The peak stagnation pressure ratio and peak temperature efficiencies were the same as configuration C tested with a Freon-12 medium. At 100-percent design speed and above, the flat operating range decreases appreciably as was noted in configuration C tests with a Freon-12 medium. However, the static pressure distribution was approximately the same as the distribution found for configuration C tested with a Freon-12 medium.

The solidity of rotor number one was reduced for configuration E with the expectation that this would increase the weight flow operating range of the compressor. The lower solidity rotor should have a greater variation in deviation angle and hence delay stall of the rear stages at the low weight flows. The results (operating range, peak stagnation pressure ratio, and static pressure distribution) of configuration E tested with air (Fig. 18) are the same as those found for configuration D tested with air (Fig. 16). For configuration E, the torque efficiency

is presented since the temperature readings were in error. For previous configurations, where both temperature efficiency and torque efficiency were available, the torque efficiencies were approximately 4 percent lower than the temperature efficiencies. The peak torque efficiency for configuration E tests with air was 77 percent at design speed. For all the speeds the peak values were from 4 percent to 6 percent lower as compared to the temperature efficiencies presented for previous configurations. It would then seem that there was no change in the efficiency of the compressor due to the lower solidity of the first rotor. The 4-percent deficit in torque efficiency, measured by the torque coupling, can be partially attributed to the friction of the two ball bearings, three roller bearings, one thrust bearing, and three carbon seals in the assembly.

The compressor was run in the rotating stall region at the speeds where it existed. Previous tests were made with the unsteady flow as the limit. For speeds above 75 percent of design speed the unsteady flow was the surge limit but for speeds below this it was the boarder of rotating stall. The torque efficiencies for the points in the rotating stall region are presented on Figure 18(b) and faired by a dashed line.

The compressor design had a possible application to a boundary-layer suction control for a slotted throat transonic wind tunnel. In this application it would be subject to varying amounts of moisture content. To find the effect of moisture on the compressor, water was

injected in the inlet 22 inches upstream of the first rotor. Four nozzles were used at this point. Water was sprayed in at rates up to 15 percent of the mass flow with no change noted in the torque efficiency. The solid point on Figure 18(b) indicates the point of water injection. Temperature readings were not taken since there was some question as to whether all the water that was injected had evaporated at the exit of the compressor.

Configuration E was also tested with a Freon-12 medium. The overall performance (Fig. 19) was the same as other Freon-12 tests (Figs. 15 and 17), the mass flow was increased by 5 percent and the flat operating range was smaller than for air tests. The peak value of the stagnation-pressure ratio and of the temperature efficiency remained the same as for configuration C tested with air (Fig. 14). The static pressure rise had the same characteristics as other configurations (C and D) tested with Freon-12.

After the water injection tests were completed, the compressor casings showed distinct lines of boundary flow (Figs. 10(a) and 10(b)).

The following is a summary of the results:

1. A flat operating characteristic at constant speed (stagnation pressure ratio independent of mass flow over the range of the machine) was obtained by making the rotational speed equal to the change in tangential velocity through the rotor at the mean radius, with the limit of weight flow being the supersonic choking in the sixth stator.

2. An average stagnation pressure ratio of 1.217 per stage was obtained at a tip speed of 550 ft/sec and an axial velocity of 650 ft/sec.

3. Peak efficiency was nearly constant (80 to 82 percent) at all speeds from 30 to 100 percent of design speed for configuration C where design conditions were met.

4. The effect of running this compressor in Freon was to increase the mass flow by 5 percent but to decrease the range of flat operation at and above design.

5. Moisture content up to 1.5 percent of the mass flow at design speed had no effect on the torque efficiency or mass flow.

The conclusions drawn from these results will be presented in the next section.

VII. CONCLUSIONS

A six-stage axial-flow compressor with a 550 foot per second tip speed and a flat operating characteristic (constant stagnation-pressure ratio at constant speed over the operating range of the compressor) was designed and tested. The design specific weight flow was 21.3 pounds per second per square foot of frontal area with an atmospheric discharge at an overall stagnation-pressure ratio of 3.25 and an inlet hub-tip radius ratio of 0.7. The compressor was designed by conventional methods. The following conclusions were drawn from the test results.

1. Impulse-type blades are suitable for low speed multistage compressors if the static-pressure rise is great enough to permit multistaging.

2. A flat operating characteristic can be designed for by using symmetrical vector diagrams and a high hub-tip radius ratio.

3. Usual limits of static-pressure coefficient were found to be applicable for this type of design.

VIII. ACKNOWLEDGMENTS

The author wishes to express his appreication to the National Advisory Committee for Aeronautics for the use of their equipment and personnel in carrying out this research project.

He also wishes to thank Mr. Willard R. Westphal of the NACA for his ideas leading to the design of this compressor and his guidance in the testing and reduction of data of this compressor, and Assistant Professor James B. Eades, Jr. and other members of the Aeronautical Engineering staff of Virginia Polytechnic Institute for their assistance in the preparation of this thesis.

IX. BIBLIOGRAPHY

1. A discussion led by Moult, E. S., and Pearson, H.: The Relative Merits of Centrifugal and Axial Compressors for Aircraft Gas Turbines. The Journal of the Royal Aeronautical Society, March 1951, p. 129.

2. Erwin, John R., and Schulze, Wallace M.: Investigation of an Impulse Axial-Flow Compressor. NACA RM L9J05a, 1950.

3. Schulze, Wallace M., Erwin, John R., and Westphal, Willard R.: Investigation of an Impulse Axial-Flow Compressor Rotor Over a Range of Blade Angles. NACA RM L50F27a, 1950.

4. Savage, Melvyn: Analysis of Aerodynamic Blade-Loading Limit Parameters for NACA 65-($C_{l_0}A_{10}$)10 Compressor-Blade Sections at Low Speeds. NACA RM L54I02a, 1955.

5. Felix, A. Richard: Summary of 65-Series Compressor-Blade Low-Speed Cascade Data by Use of the Carpet-Plotting Technique. NACA TN 3913, 1957. (Supersedes NACA RM L54H18a.)

6. Goldberg, Theordore J., Boxer, Emanuel, and Bernot, Peter T.: Experimental Investigation of an Axial-Flow Supersonic Compressor Having Rounded Leading-Edge Blades With an 8-Percent Mean Thickness-Chord Ratio. NACA RM L53G16, 1953.

7. Huber, Paul W., and Kantrowitz, Arthur: A Device for Measuring Sonic Velocity and Compressor Mach Number. NACA TN 1664, 1948.

8. Boxer, Emanuel, and Erwin, John R.: Investigation of a Shrouded and an Unshrouded Axial-Flow Supersonic Compressor. NACA RM L50F05, 1950.

X. VITA

The author was born in Concord, New Hampshire, on September 2, 1930. He graduated from the Concord High School in Concord, New Hampshire in 1948. Upon graduation from high school he entered the University of New Hampshire in Durham, New Hampshire and received the degree of Bachelor of Science in Mechanical Engineering in 1952. Since that time he has been employed as an Aeronautical Research Engineer by the National Advisory Committee for Aeronautics at Langley Field, Virginia.

XI. APPENDICES

Appendix A. Derivation of an Equation for the Rate of Change of Work Input With a Change in Axial Velocity

A typical velocity diagram is shown in sketch 1.

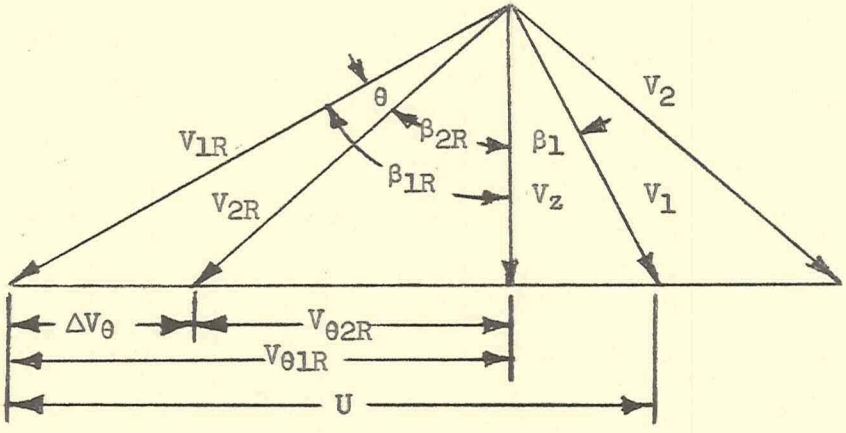

Sketch 1

It is assumed that:

1. Entering and leaving axial velocities are equal.
2. Streamlines remain at the same radii.
3. Leaving flow direction relative to the rotor remains constant as the entering flow direction varies.

The work done per unit mass flow is $U\Delta V_\theta$, while the change in tangential velocity is

$$\Delta V_\theta = V_{\theta 1R} - V_{\theta 2R} \qquad \text{(A1)}$$

or

$$\Delta V_\theta = U - V_z \tan \beta_1 - V_z \tan \beta_{2R} \qquad \text{(A2)}$$

Differentiating the change in tangential velocity with respect to the axial velocity gives

$$\frac{d(\Delta V_\theta)}{dV_z} = -(\tan \beta_1 + \tan \beta_{2R}) \tag{A3}$$

Multiplying both sides of equation (A3) by $V_z/\Delta V_\theta$ gives

$$\frac{\dfrac{d(\Delta V_\theta)}{\Delta V_\theta}}{\dfrac{dV_z}{V_z}} = \frac{-(V_z \tan \beta_1 + V_z \tan \beta_{2R})}{\Delta V_\theta} \tag{A4}$$

Simplifying equation (A4) by use of equation (A2) gives

$$\frac{\dfrac{d(\Delta V_\theta)}{\Delta V_\theta}}{\dfrac{dV_z}{V_z}} = \frac{\Delta V_\theta - U}{\Delta V_\theta} \tag{A5}$$

or

$$\frac{\dfrac{d(\Delta V_\theta)}{\Delta V_\theta}}{\dfrac{dV_z}{V_z}} = 1 - \frac{U}{\Delta V_\theta} \tag{A6}$$

Equation (A6) is an expression for the rate of change of work input with a change in axial velocity at a constant rotational speed.

Appendix B. Effect of Testing With Freon-12

The increase in density will allow the compressor to operate with an effective area change without a change in geometry. To illustrate this the percentage increase in density is computed.

The work input can be written as

$$\text{Work} = mc_p(T_2 - T_1) = mU\Delta V_\theta \tag{B1}$$

Equation (B1) can be rewritten in the form of temperature ratio

$$\frac{T_2}{T_1} = \left(\frac{U\Delta V_\theta}{c_p T_1} + 1\right) \tag{B2}$$

Now assuming the compressor operates with a polytropic process, then the following expression

$$\frac{T_2}{T_1} = \left(\frac{P_2}{P_1}\right)^{\frac{(n-1)}{n}} = \left(\frac{\rho_2}{\rho_1}\right)^{(n-1)} \tag{B3}$$

can be used to relate the stagnation values of pressure, density, and temperature.

The relation for stagnation-pressure ratio in terms of velocity and inlet temperature can be found by combining equations (B3) and (B2). This will result in

$$\frac{P_2}{P_1} = \left(\frac{U\Delta V_\theta}{c_p T_1} + 1\right)^{\frac{n}{(n-1)}} \tag{B4}$$

From equation (B4), the stagnation-pressure ratio is ratio of air to Freon-12

$$\frac{\left(\frac{P_2}{P_1}\right)_{air}}{\left(\frac{P_2}{P_1}\right)_{Freon\text{-}12}} = \frac{\left(\frac{U\Delta V_\theta}{c_p T_1} + 1\right)^{\frac{n}{(n-1)}}}{\left(\frac{U\Delta V_\theta}{c_p T_1} + 1\right)^{\frac{n}{(n-1)}}} \tag{B5}$$

Equation (B3) gives the relation between the stagnation-pressure ratio and the stagnation-density ratio. This can be written in the air to Freon-12 ratio as

$$\frac{\left(\frac{\rho_2}{\rho_1}\right)_{air}}{\left(\frac{\rho_2}{\rho_1}\right)_{Freon\text{-}12}} = \frac{\left(\frac{P_2}{P_1}\right)_{air}^{1/n}}{\left(\frac{P_2}{P_1}\right)_{Freon\text{-}12}^{1/n}} \tag{B6}$$

The ratio of the tip speeds for the same relative inlet Mach number in air and Freon-12, assuming no inlet whirl, is, from reference 8,

$$\frac{U_{air}}{U_{Freon\text{-}12}} = \left[\frac{\left(\frac{\gamma R}{2 + (\gamma - 1)M_1^2}\right)_{air}}{\left(\frac{\gamma R}{2 + (\gamma - 1)M_1^2}\right)_{Freon\text{-}12}} \right] \tag{B7}$$

where R in this equation is the universal gas constant.

For a multistage compressor with a symmetrical vector diagram, where all stages turn the flow axial, and the work input is constant per stage regardless of the output of the previous stage, the above equations can

be used. The overall stagnation-pressure ratio can be computed without a stage-by-stage analysis since $U = \Delta V_\theta$. Assuming a polytropic efficiency of 85.8 percent and an inlet absolute Mach number of 0.6, equation (B5) can be evaluated for the design conditions of the subject compressor. The resulting ratio is

$$\frac{\left(\frac{P_4}{P_1}\right)_{air}}{\left(\frac{P_4}{P_1}\right)_{Freon\text{-}12}} = \frac{\left(\frac{U^2}{c_p T_1} + 1\right)^{3.0}}{\left(\frac{U^2}{c_p T_1} + 1\right)^{7.7}} = 1.025 \qquad (B8)$$

This indicates the pressure ratio should be 2.5 percent less in Freon-12 for design efficiency. For an air design pressure ratio of 3.25, equation (B6) results in

$$\frac{\left(\frac{\rho_4}{\rho_1}\right)_{Freon\text{-}12}}{\left(\frac{\rho_4}{\rho_1}\right)_{air}} = \frac{\left(\frac{P_4}{P_1}\right)^{0.870}_{Freon\text{-}12}}{\left(\frac{P_4}{P_1}\right)^{0.667}_{air}} = 1.243 \qquad (B9)$$

The density is then approximately 24 percent greater for Freon-12 than for air at the compressor exit. This would effectively increase the effective annulus area by 24 percent without a geometrical change.

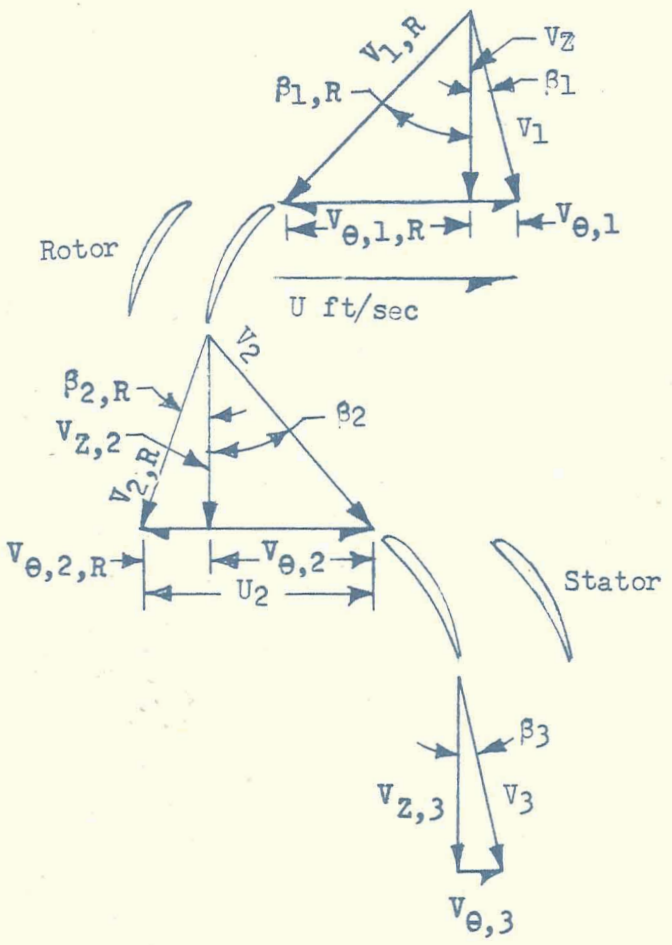

Composite diagram of the above

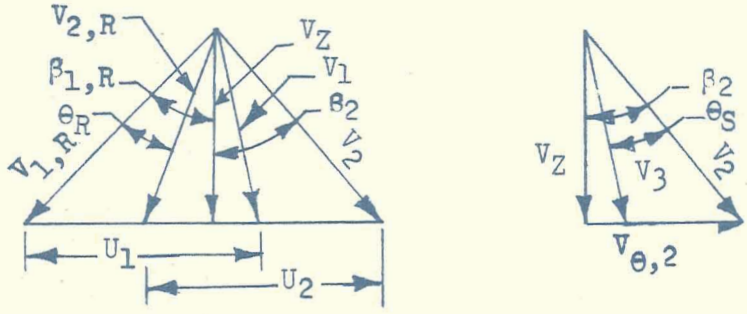

Figure 1.- General vector diagram.

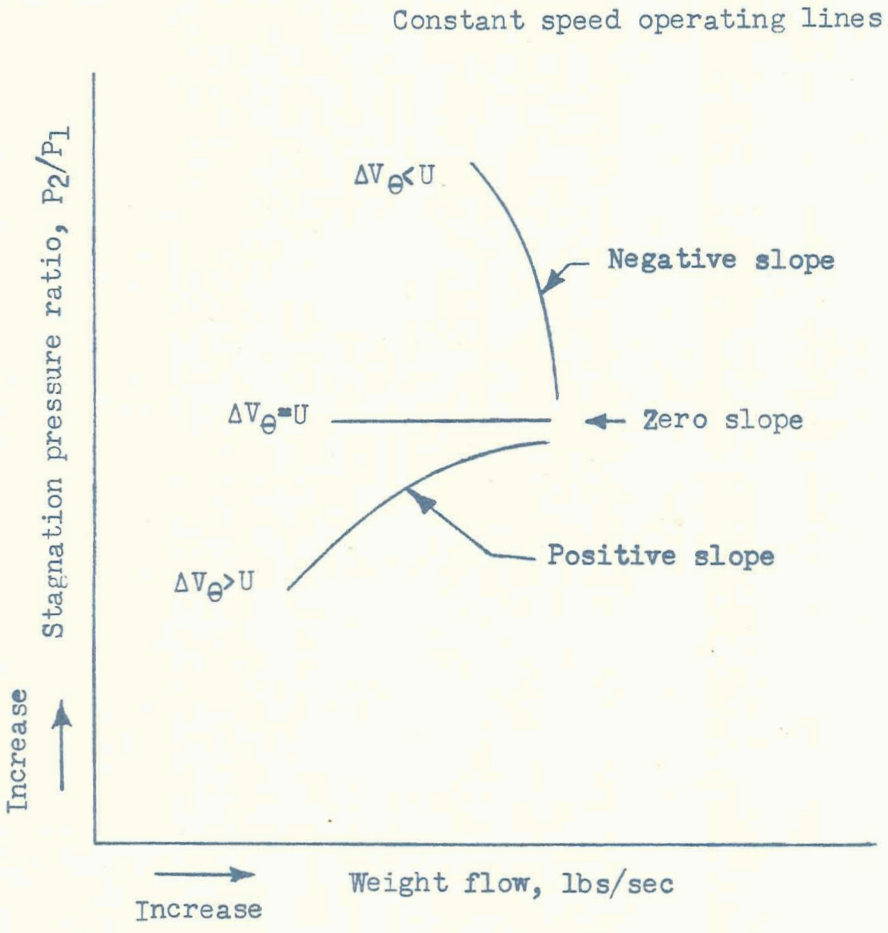

Figure 2.- Typical constant speed overall performance for three types of axial-flow compressors.

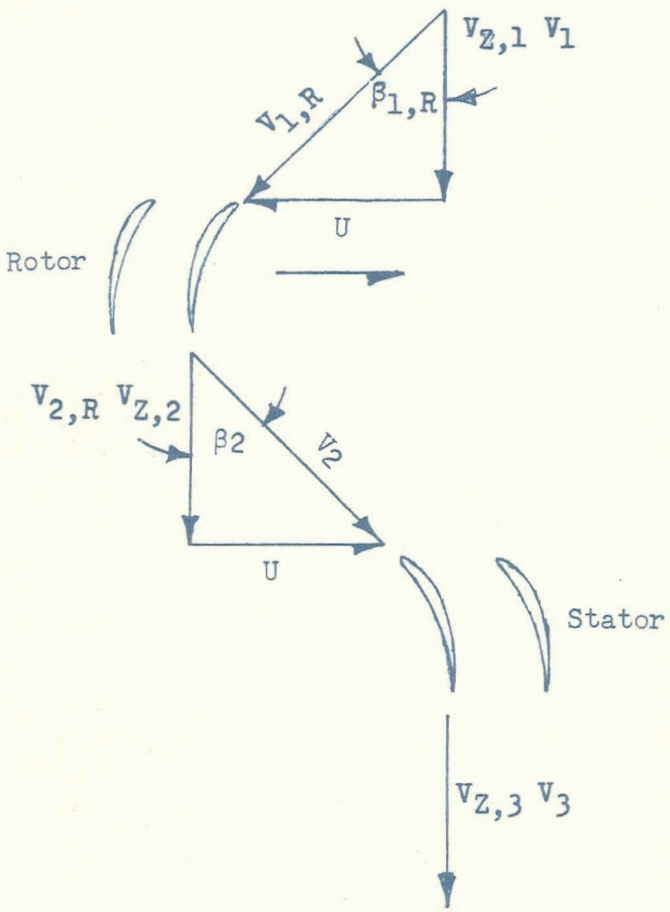

Composite diagram of the above

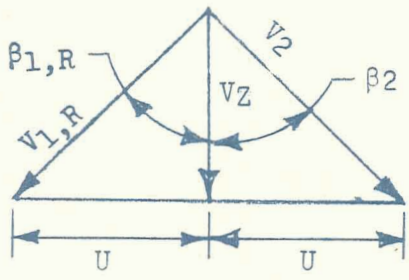

Figure 3.- Typical symmetrical vector diagram.

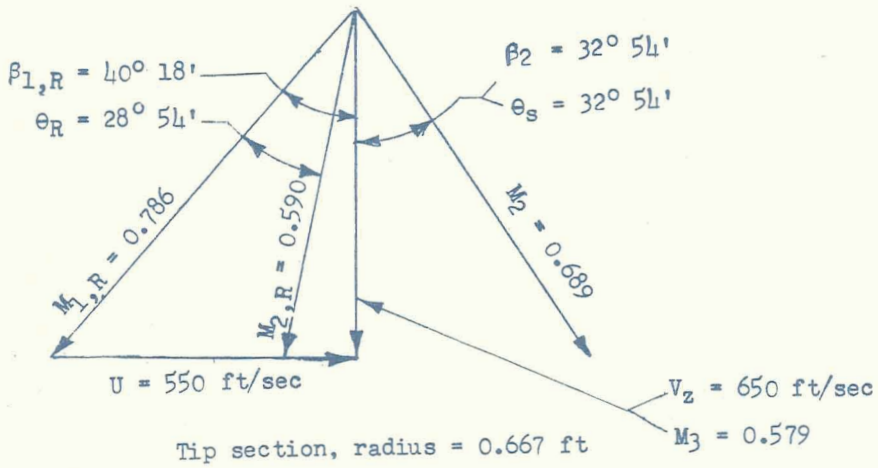

Tip section, radius = 0.667 ft

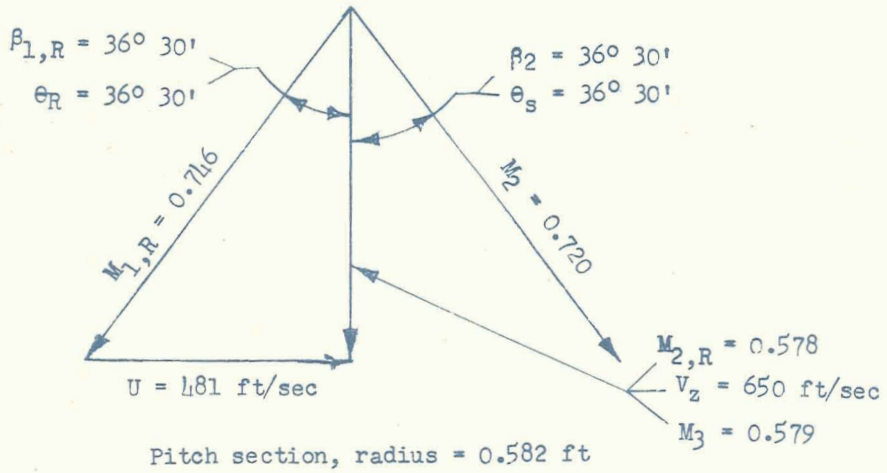

Pitch section, radius = 0.582 ft

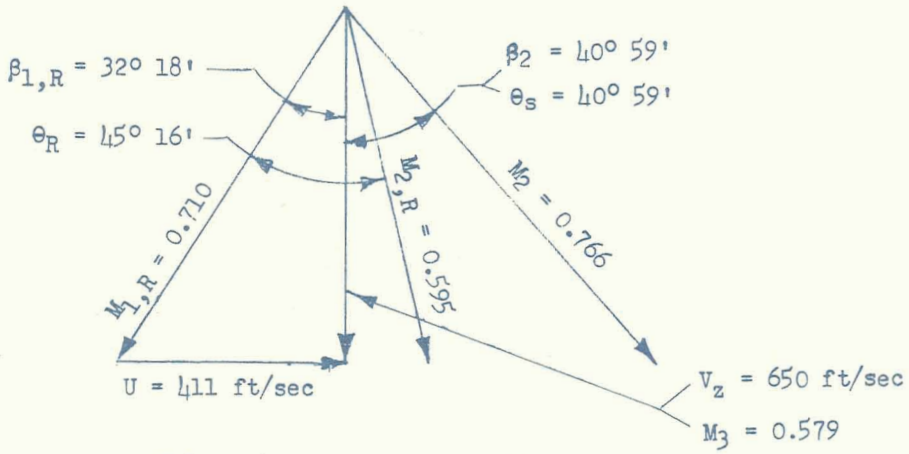

Hub section, radius = 0.498 ft

Figure 4.- Design vector diagram for first stage of six-stage compressor at several radii.

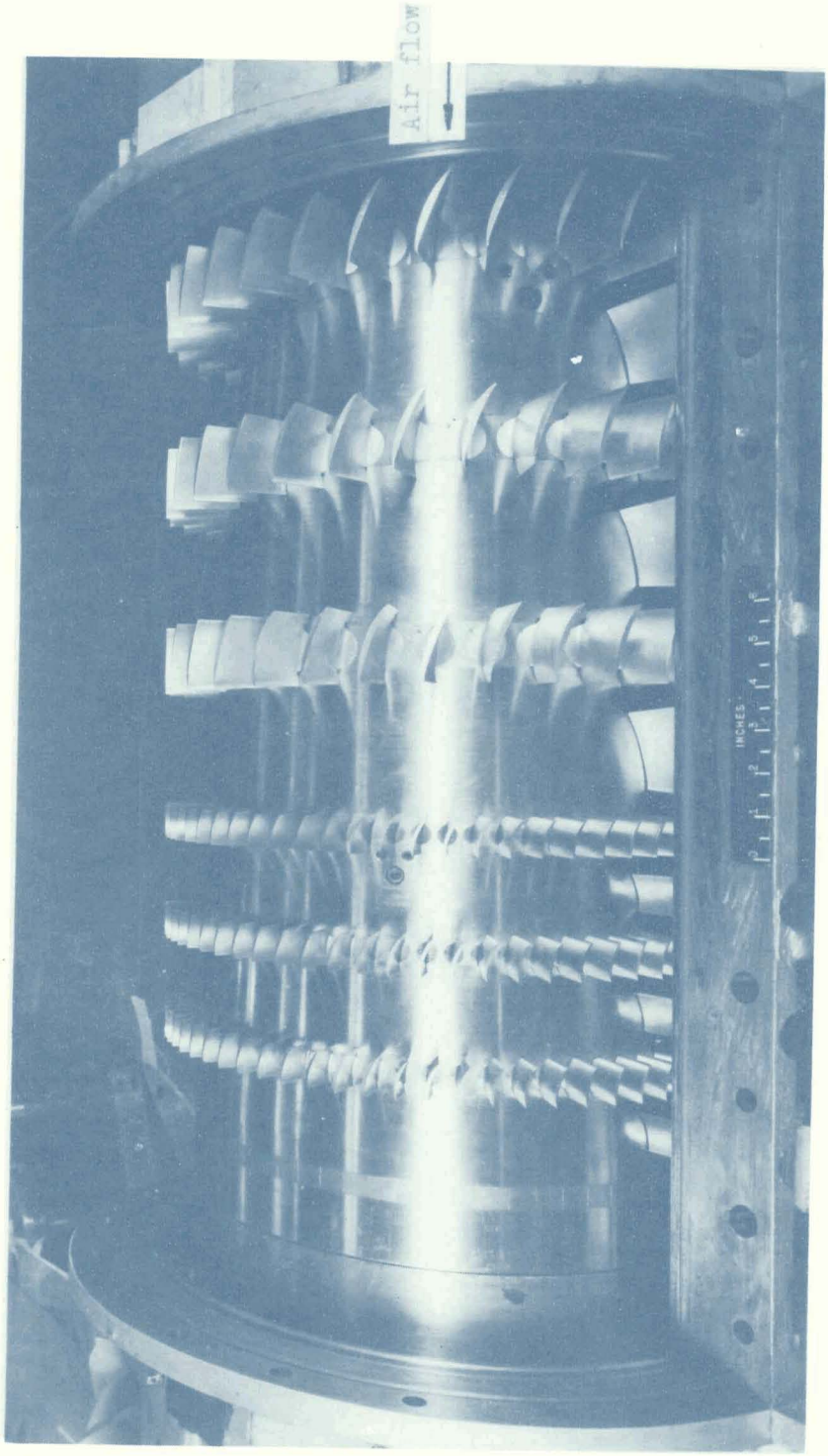

(a) Rotor assembly. L-93975.1

Figure 5.- Six-stage compressor assembly configuration A.

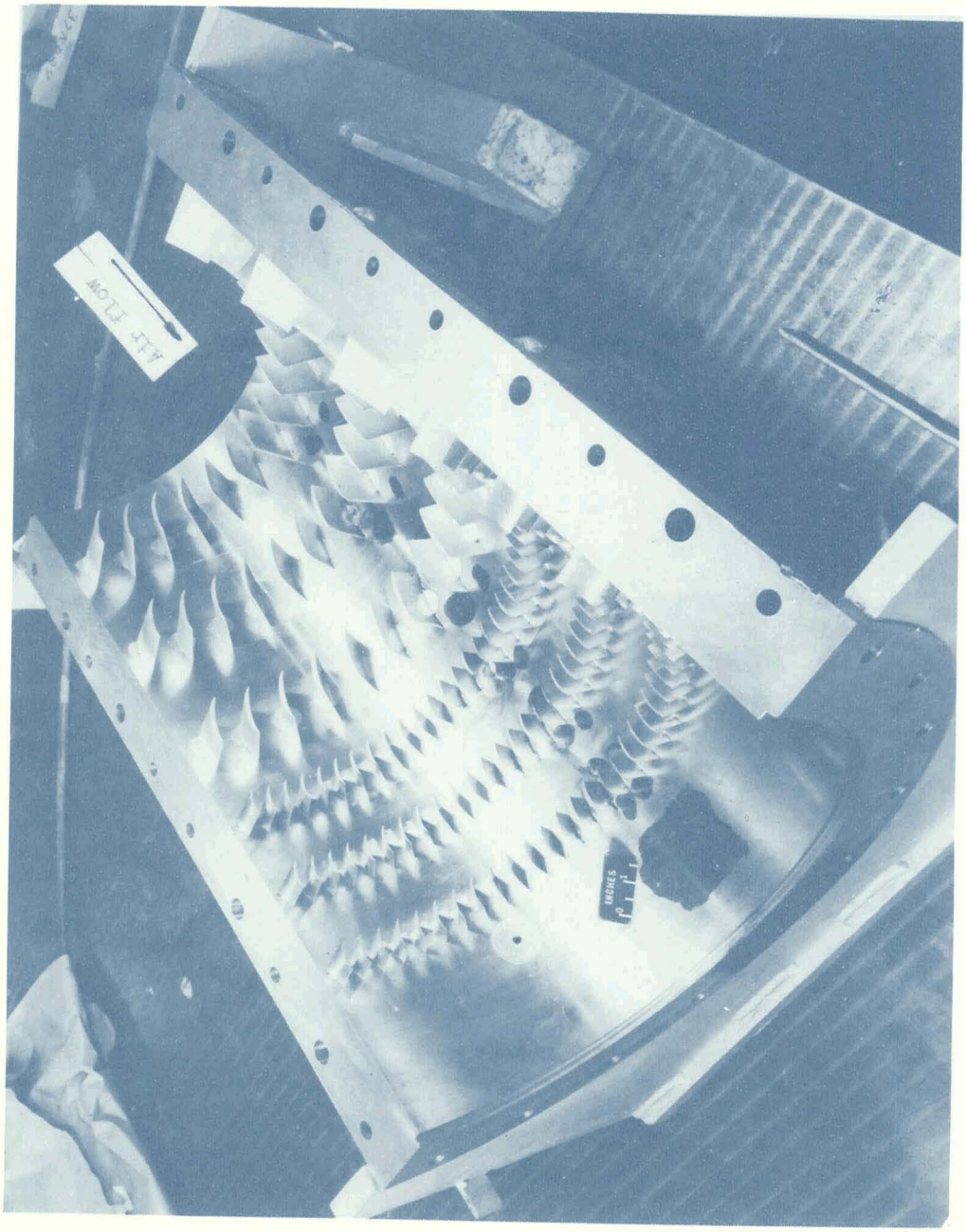

(b) Stator assembly. L-93972.1

Figure 5.- Concluded.

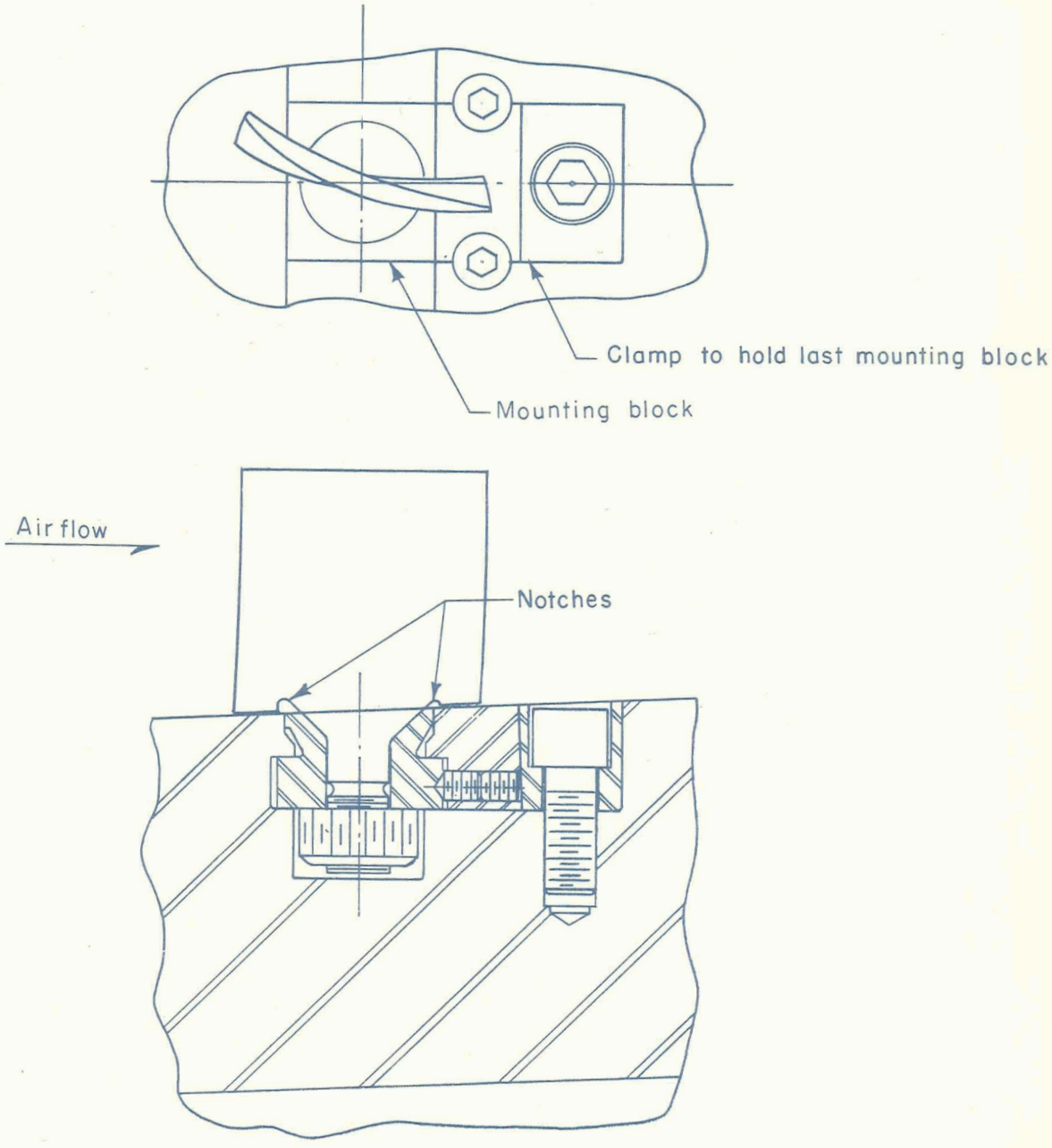

Figure 6.- Detail of blade mounting and notches in blade.

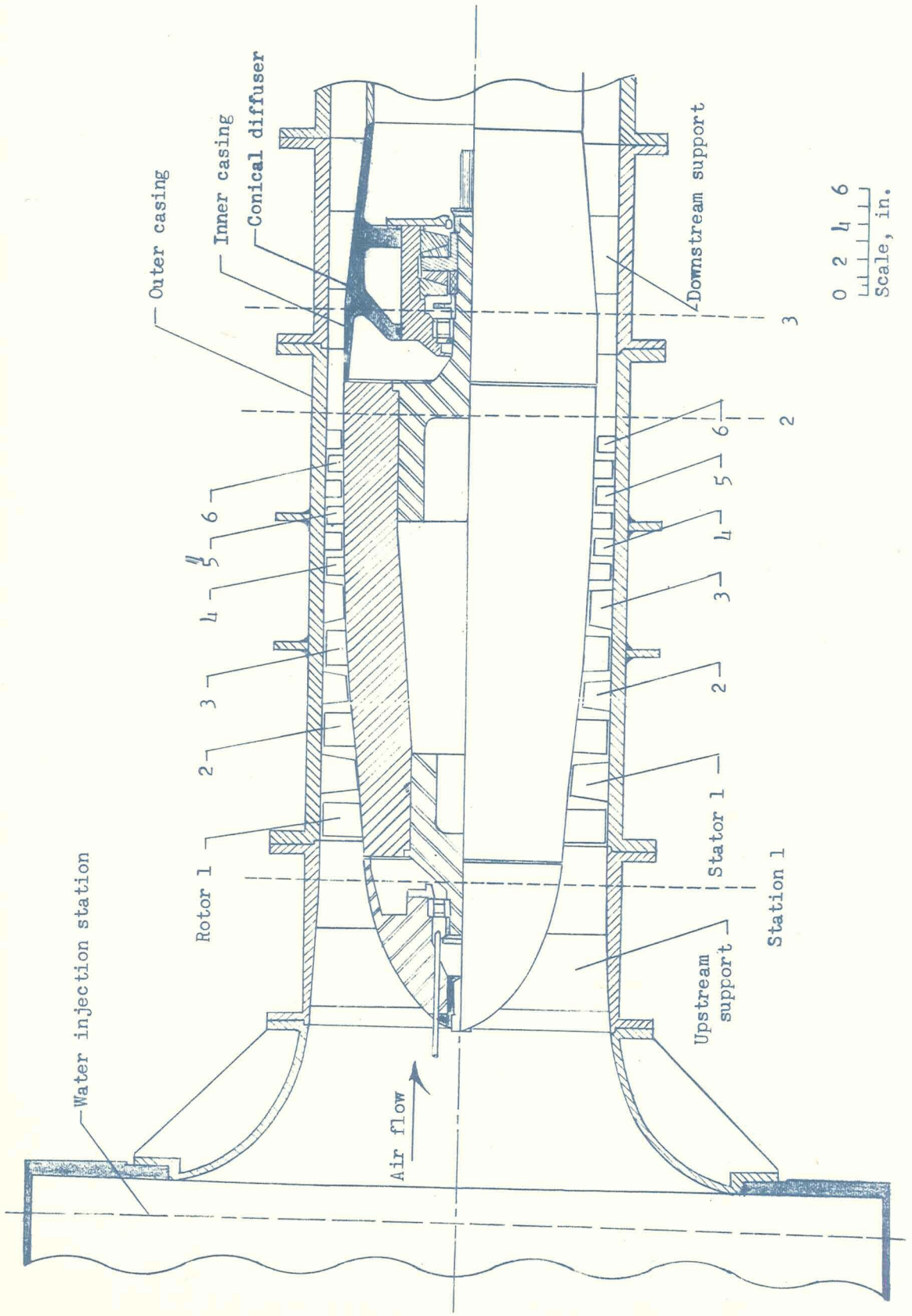

Figure 7.- Sectional view of compressor.

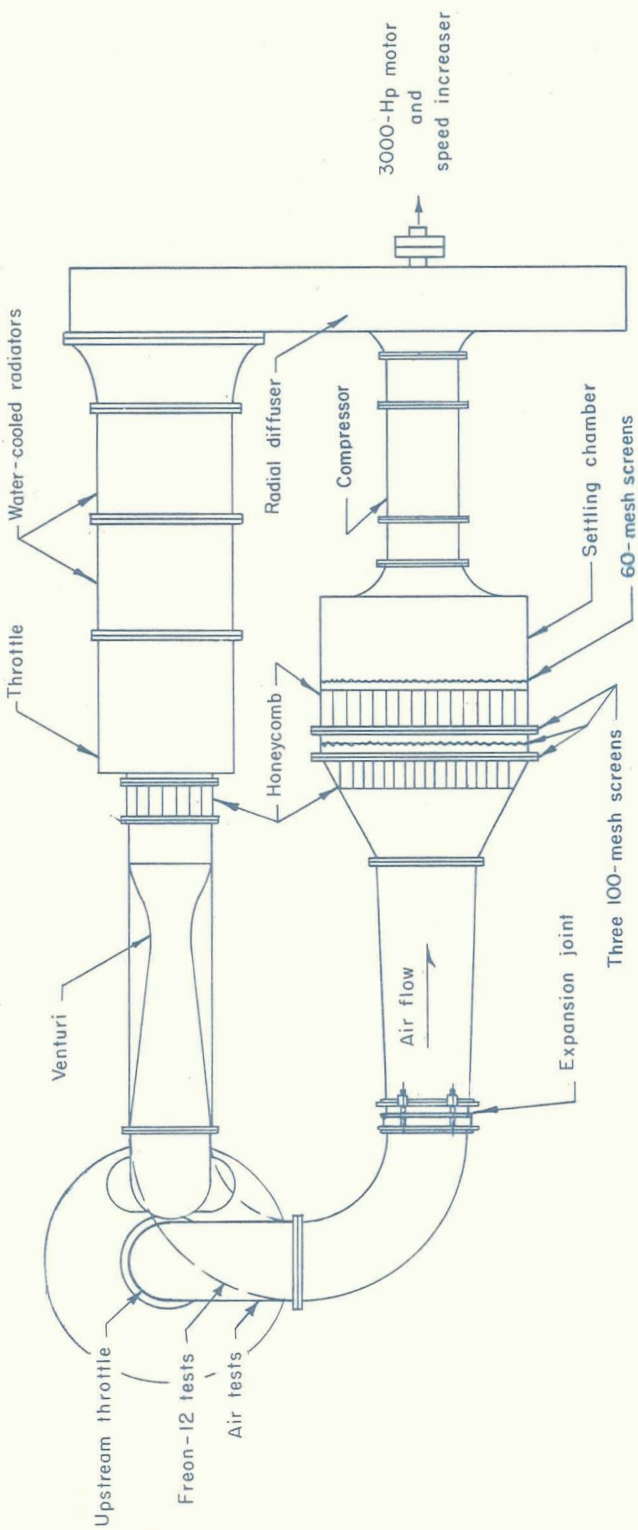

Figure 8.- Plan view of compressor test stand.

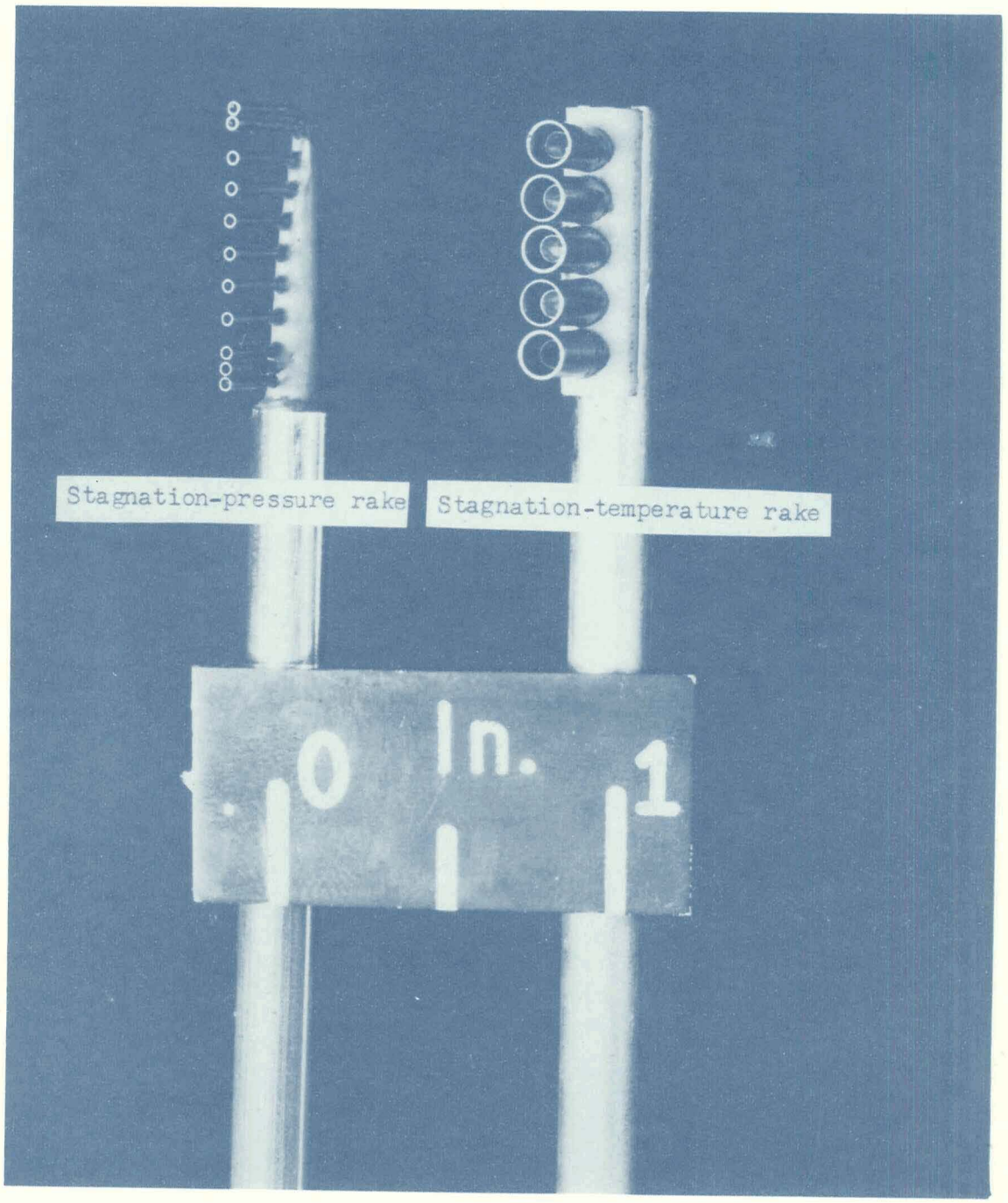

Figure 9.- Instruments. L-57-2230.1

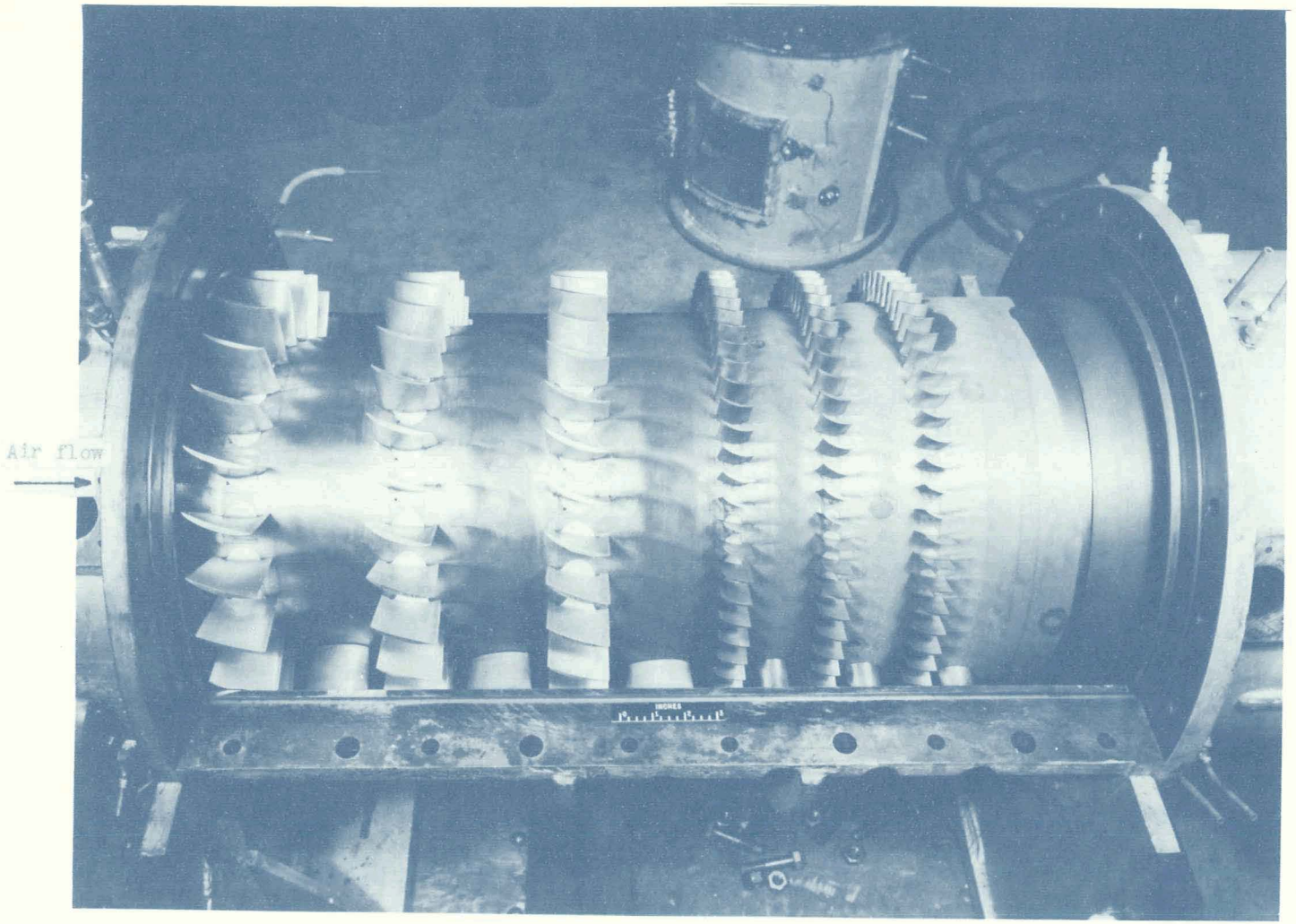

(a) Rotor assembly. L-96063.1

Figure 10.- Six-stage compressor assembly after solidity change, configuration E.

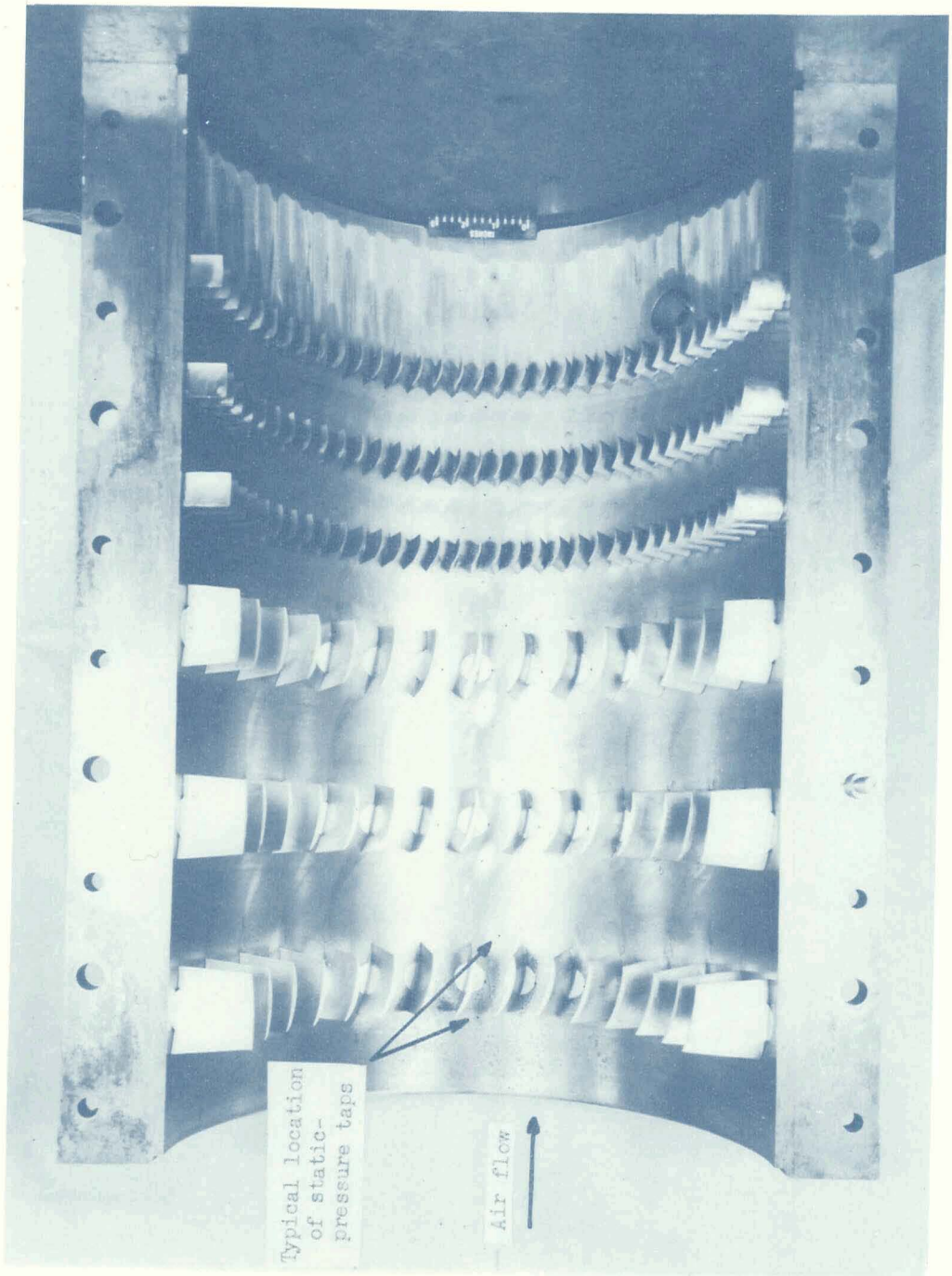

(b) Stator assembly. L-96064.1

Figure 10.- Concluded.

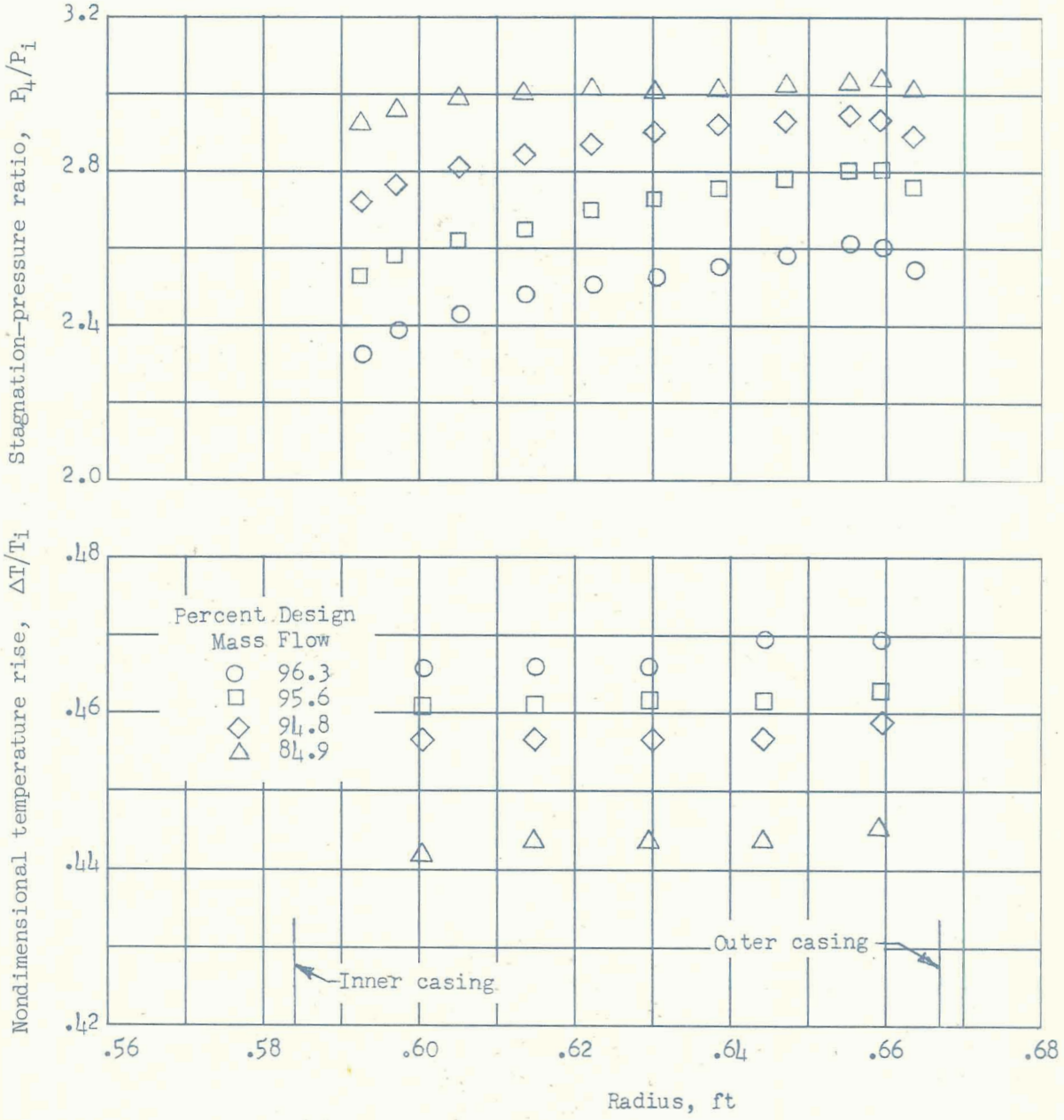

Figure 11.- Stagnation pressure and temperature distribution against radius for design speed.

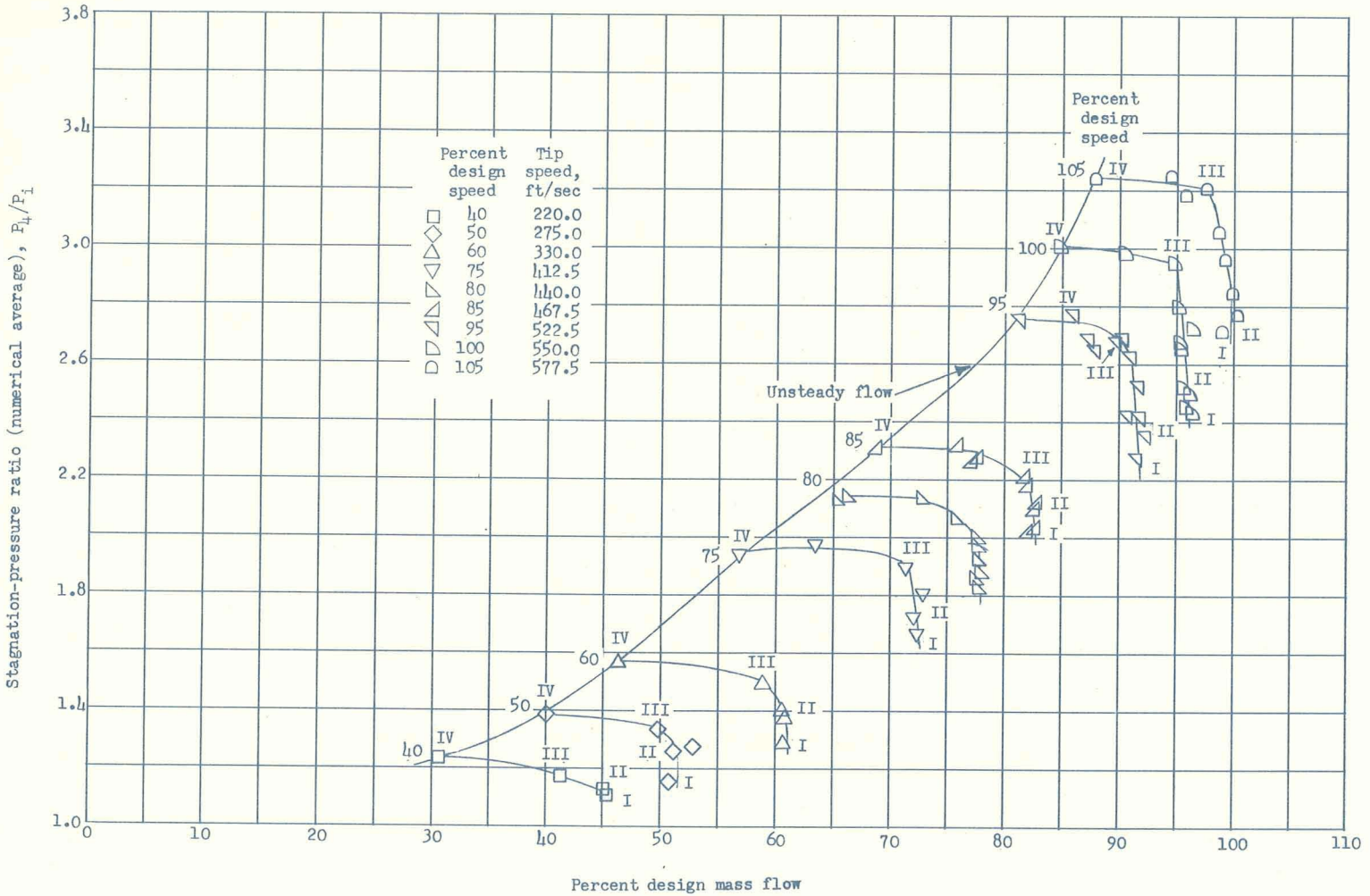

(a) Variation of stagnation-pressure ratio (numerical average) with percent of design mass flow.

Figure 12.- Overall performance of a six-stage axial-flow compressor configuration A in air.

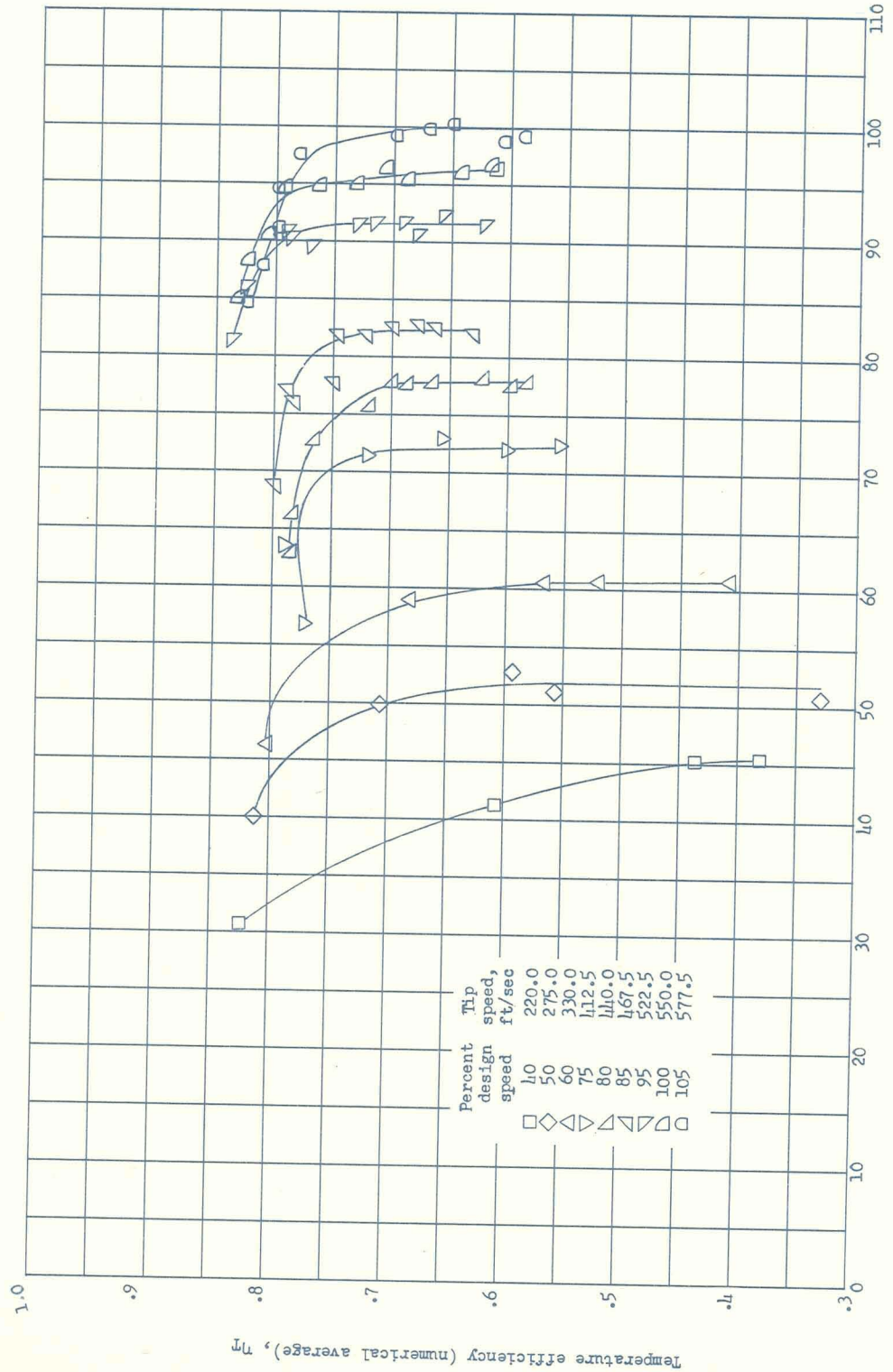

(b) Variation of temperature efficiency (numerical average) with percent of design mass flow.

Figure 12.- Continued.

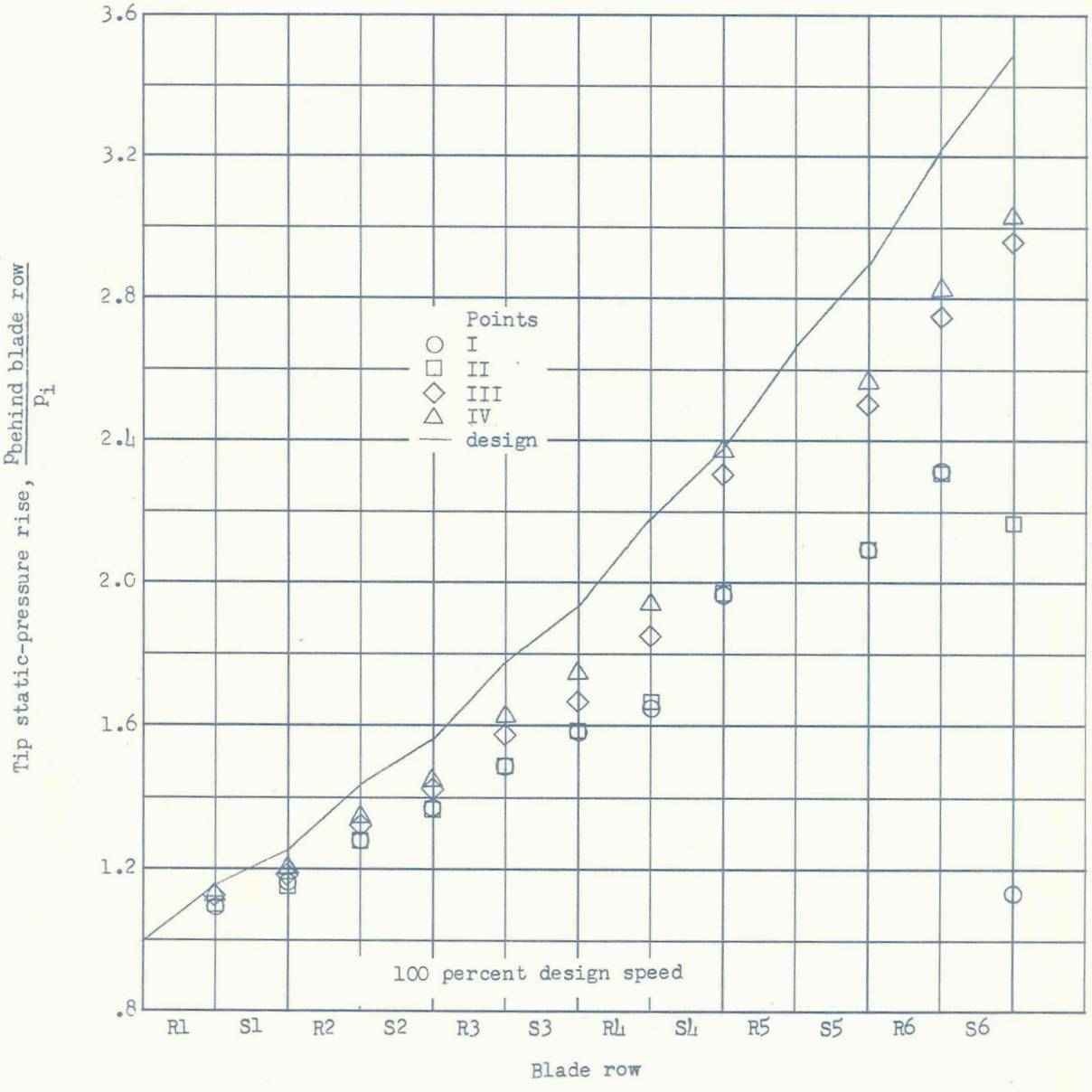

(c) Variation of tip static-pressure rise with blade row.

Figure 12.- Continued.

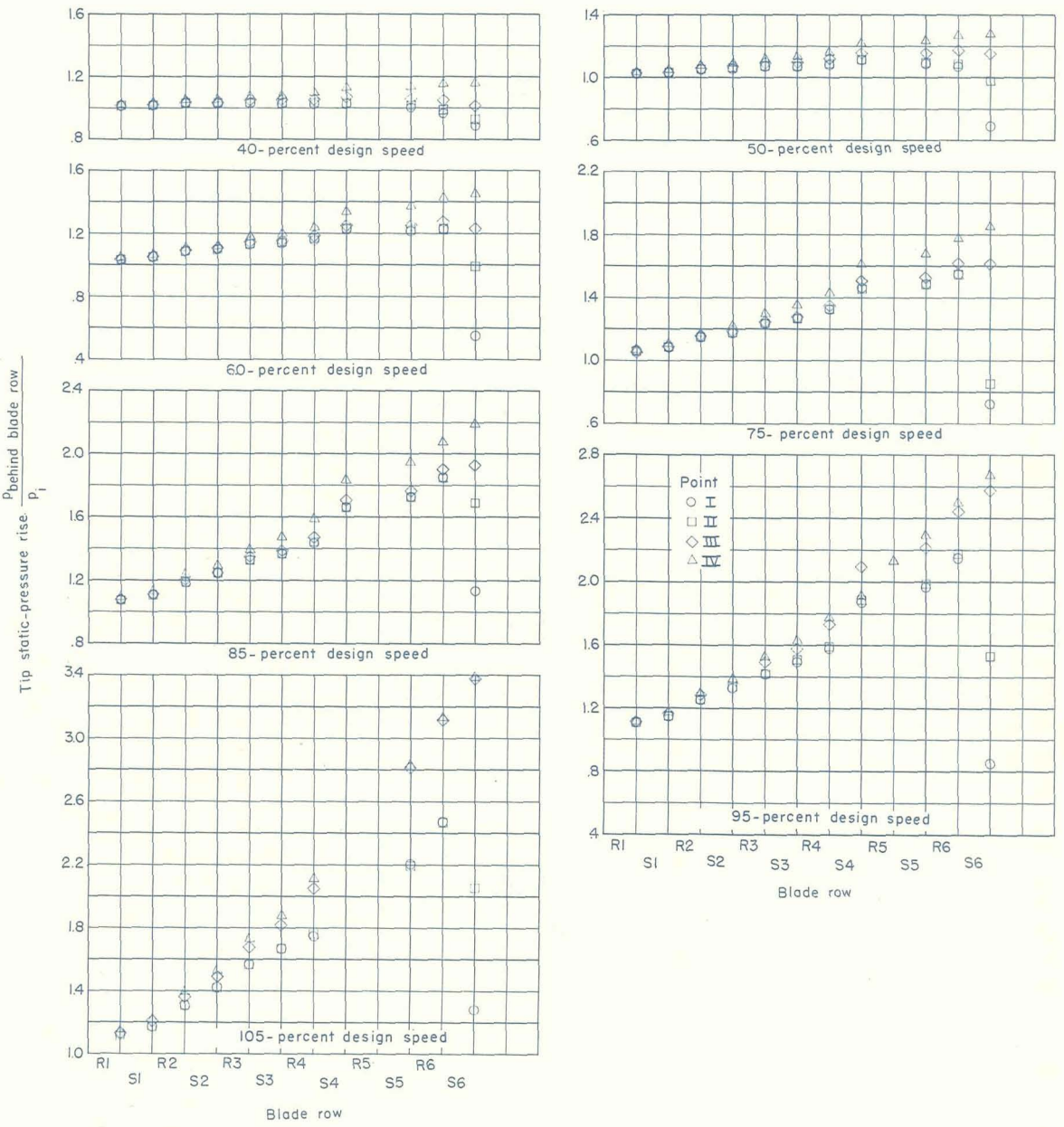

(c) Concluded.

Figure 12.- Concluded.

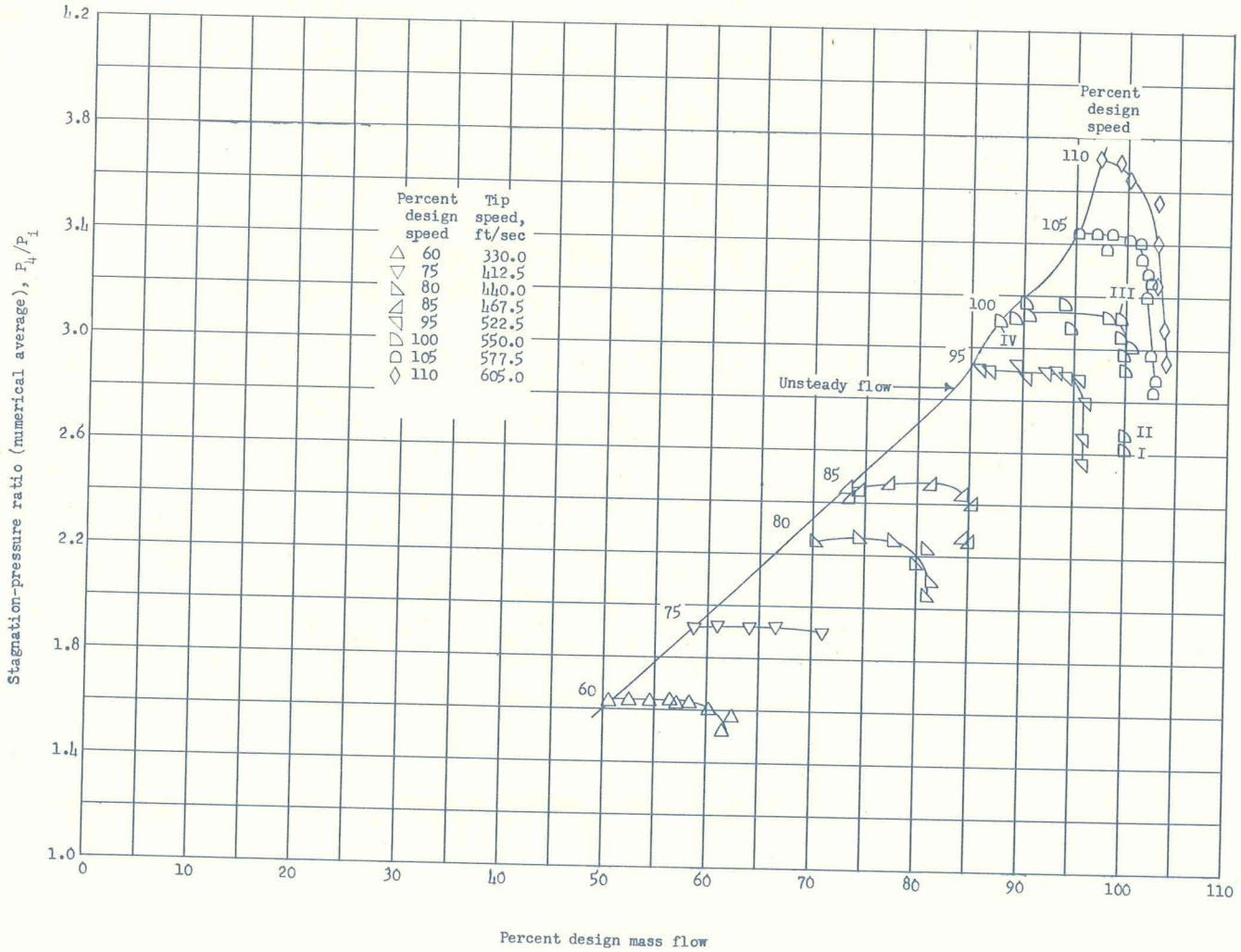

(a) Variation of stagnation-pressure ratio (numerical average) with percent of design mass flow.

Figure 13.- Overall performance of a six-stage axial-flow compressor configuration B in air.

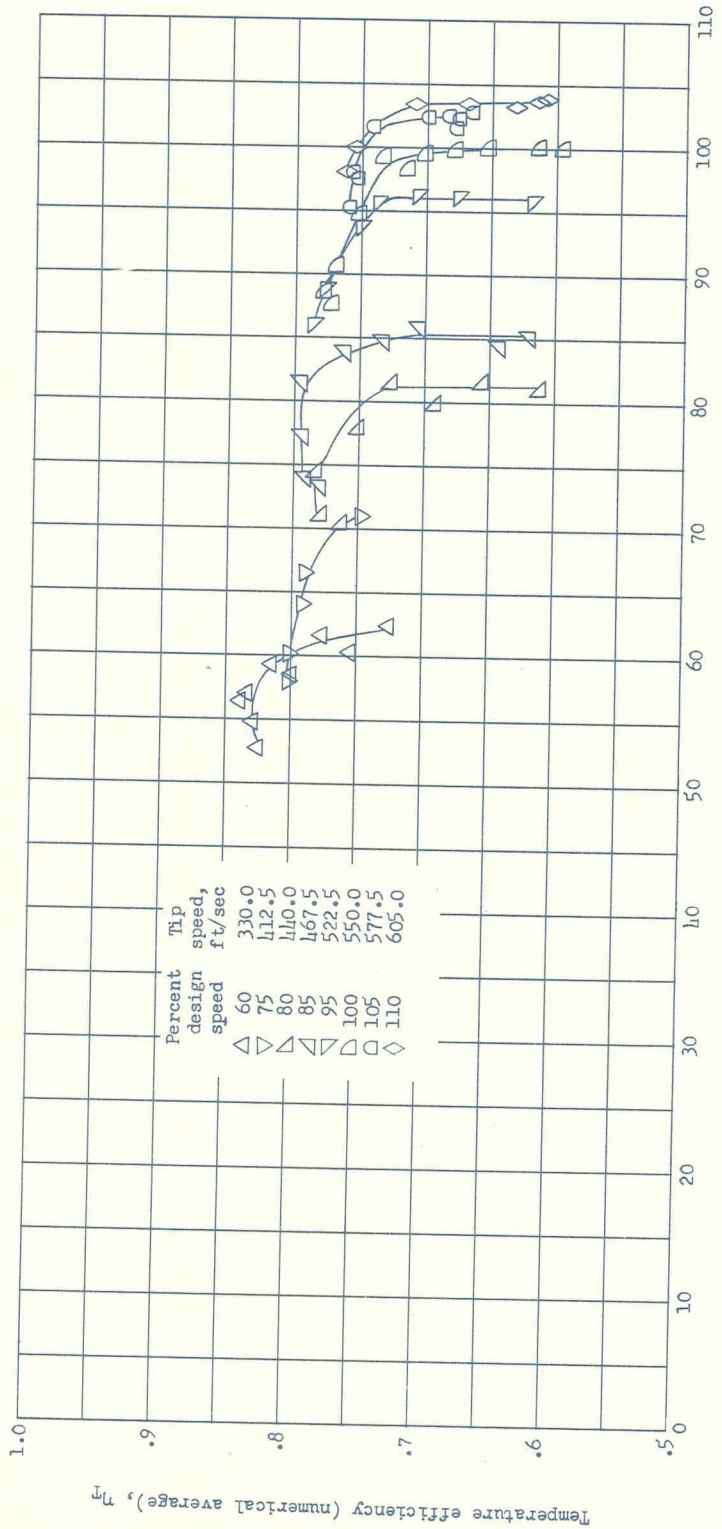

(b) Variation of temperature efficiency (numerical average) with percent of design mass flow.

Figure 13.- Continued.

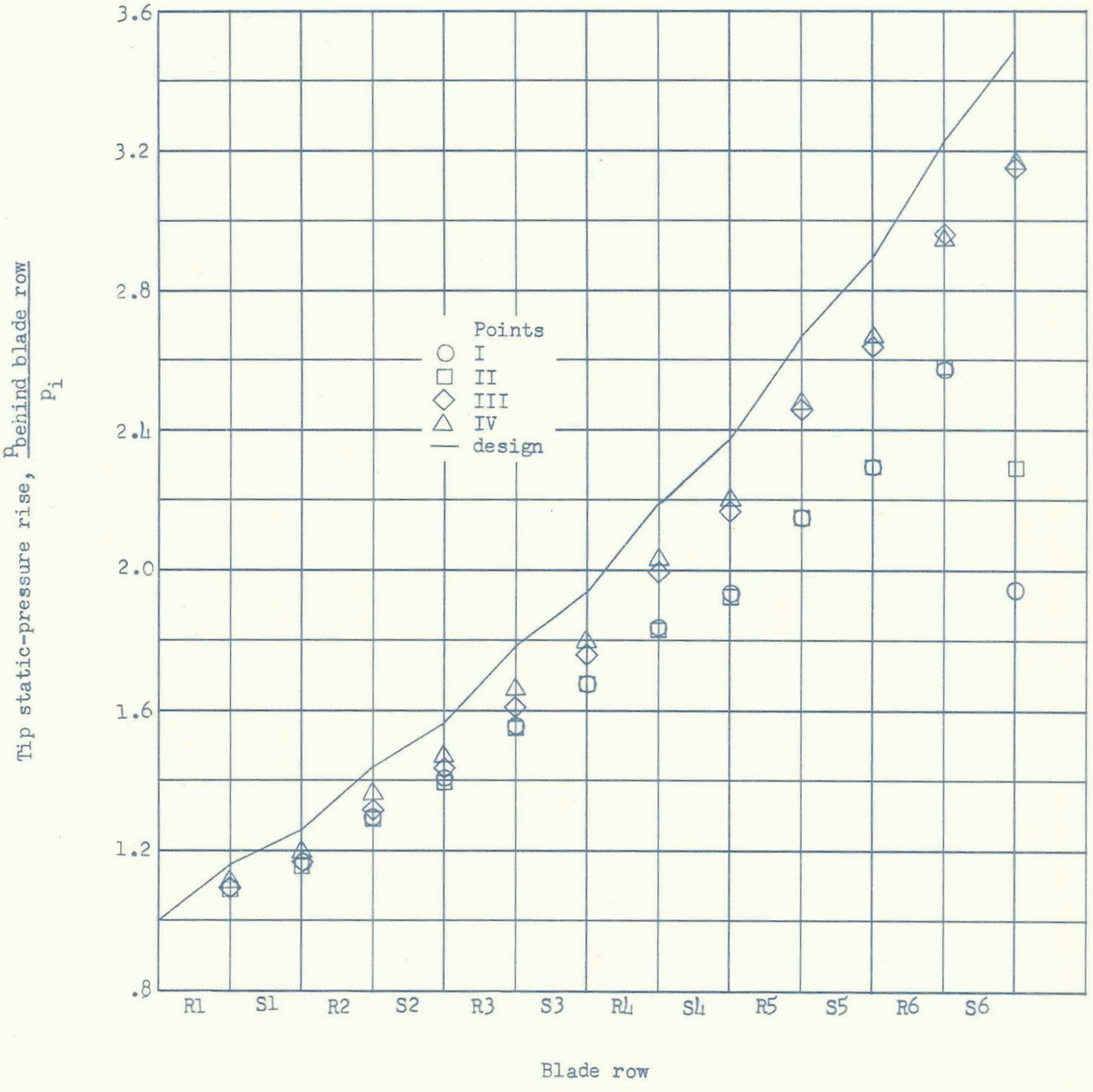

(c) Variation of tip static-pressure rise with blade row at 100-percent design speed.

Figure 13.- Concluded.

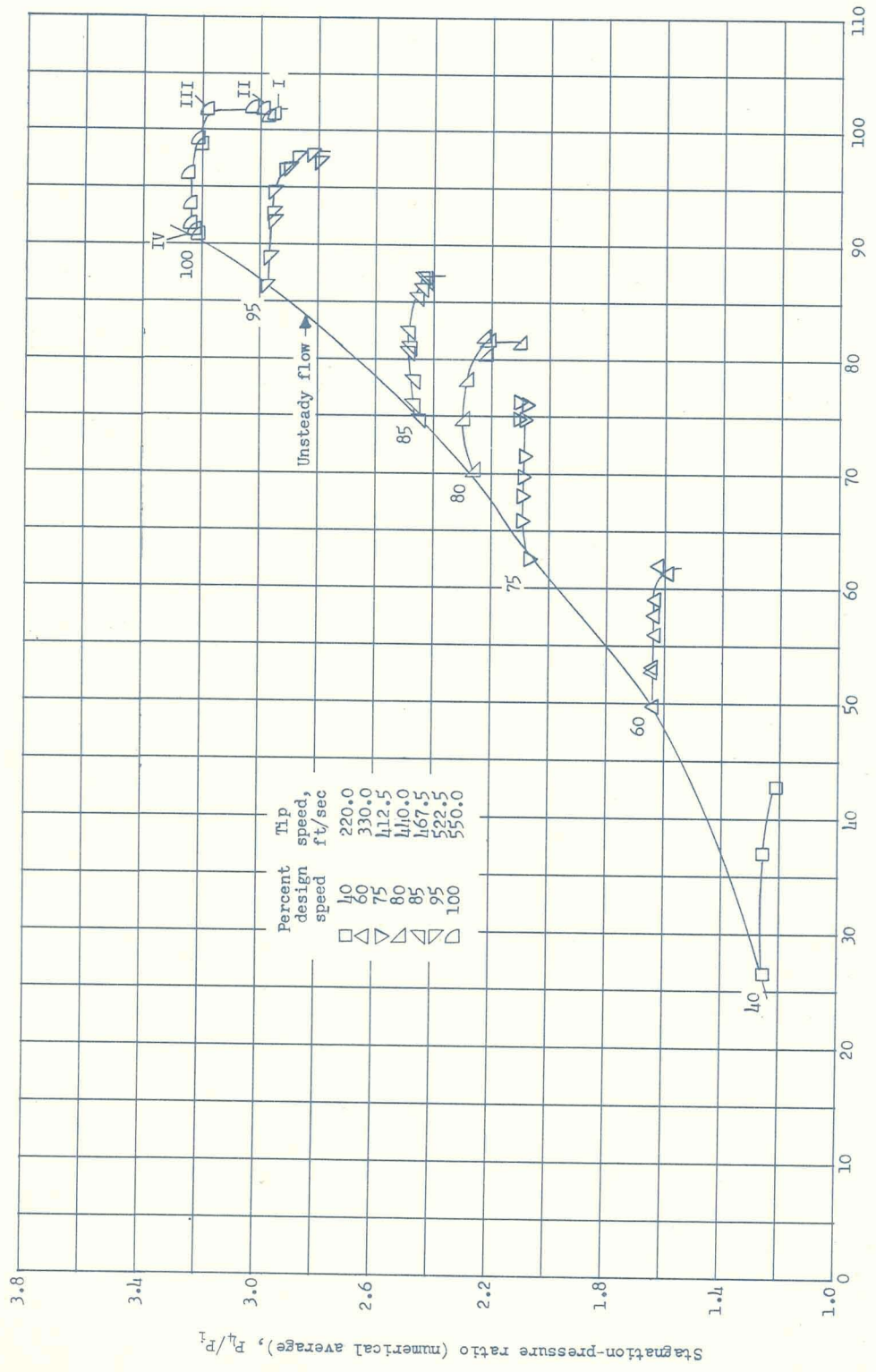

(a) Variation of stagnation-pressure ratio (numerical average) with percent of design mass flow.

Figure 14.- Overall performance of a six-stage axial-flow compressor configuration C in air.

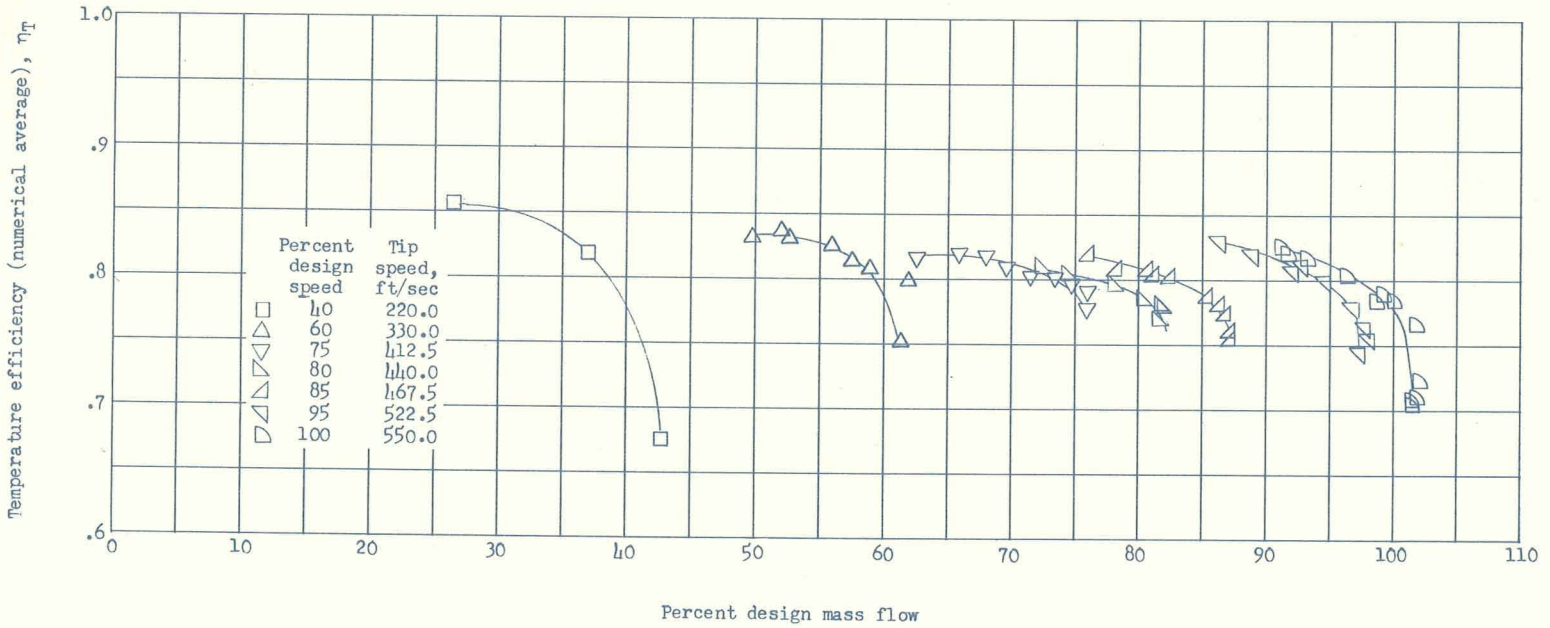

(b) Variation of temperature efficiency (numerical average) with percent of design mass flow.

Figure 14.- Continued.

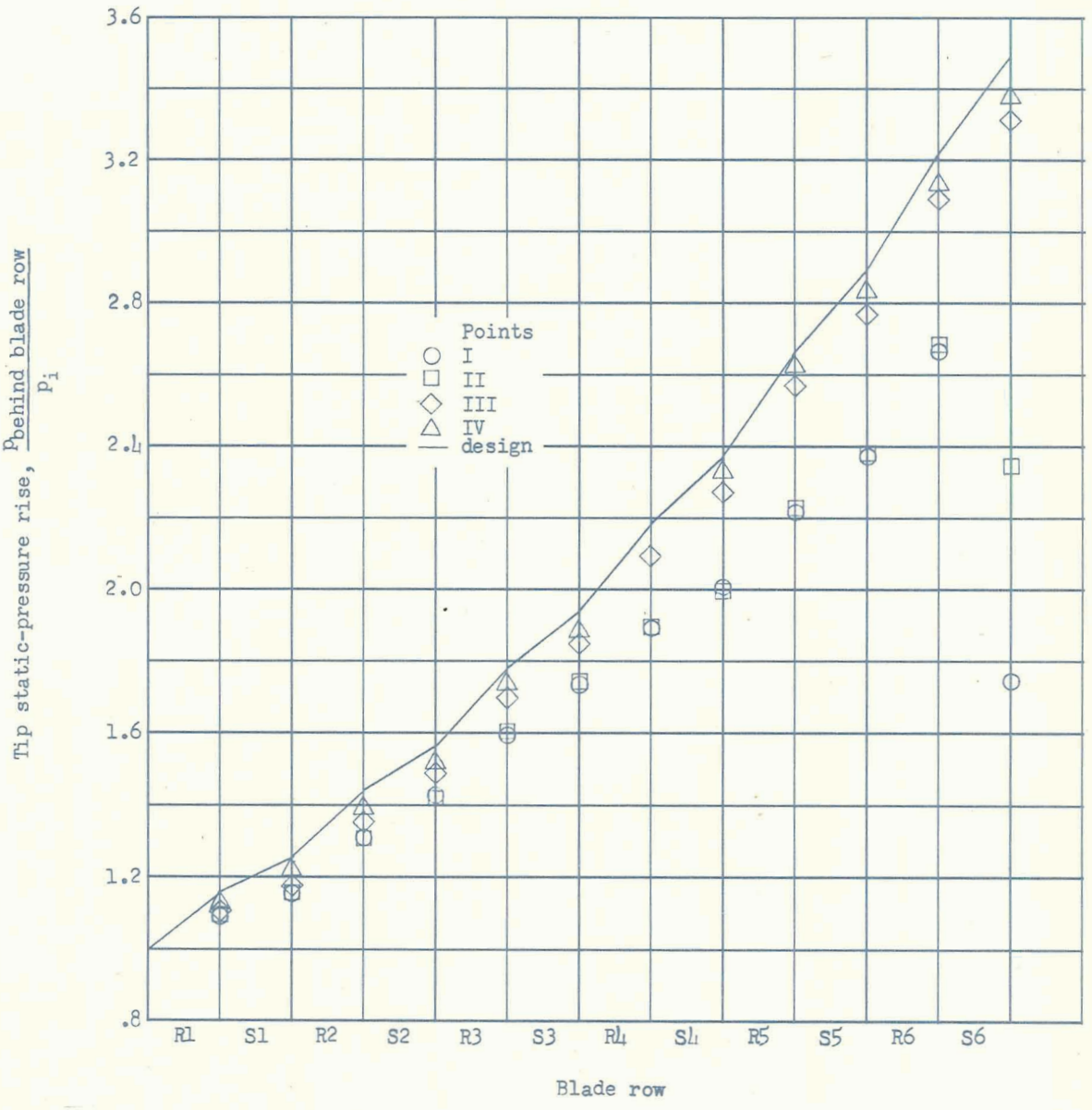

(c) Variation of tip static-pressure rise with blade row at 100-percent design speed.

Figure 14.- Concluded.

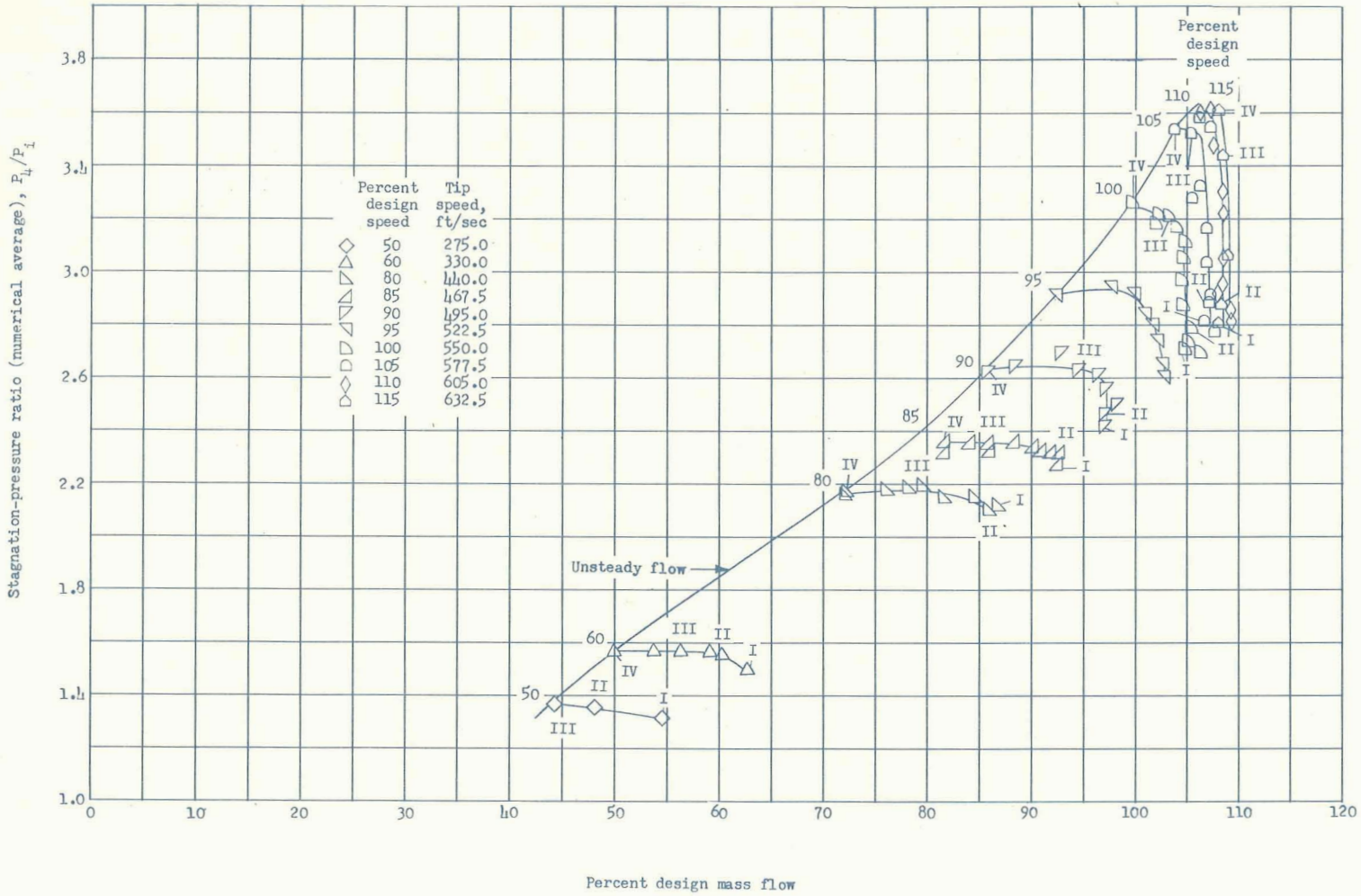

(a) Variation of stagnation-pressure ratio (numerical average) with percent of design mass flow.

Figure 15.- Overall performance of a six-stage axial-flow compressor configuration C in Freon-12.

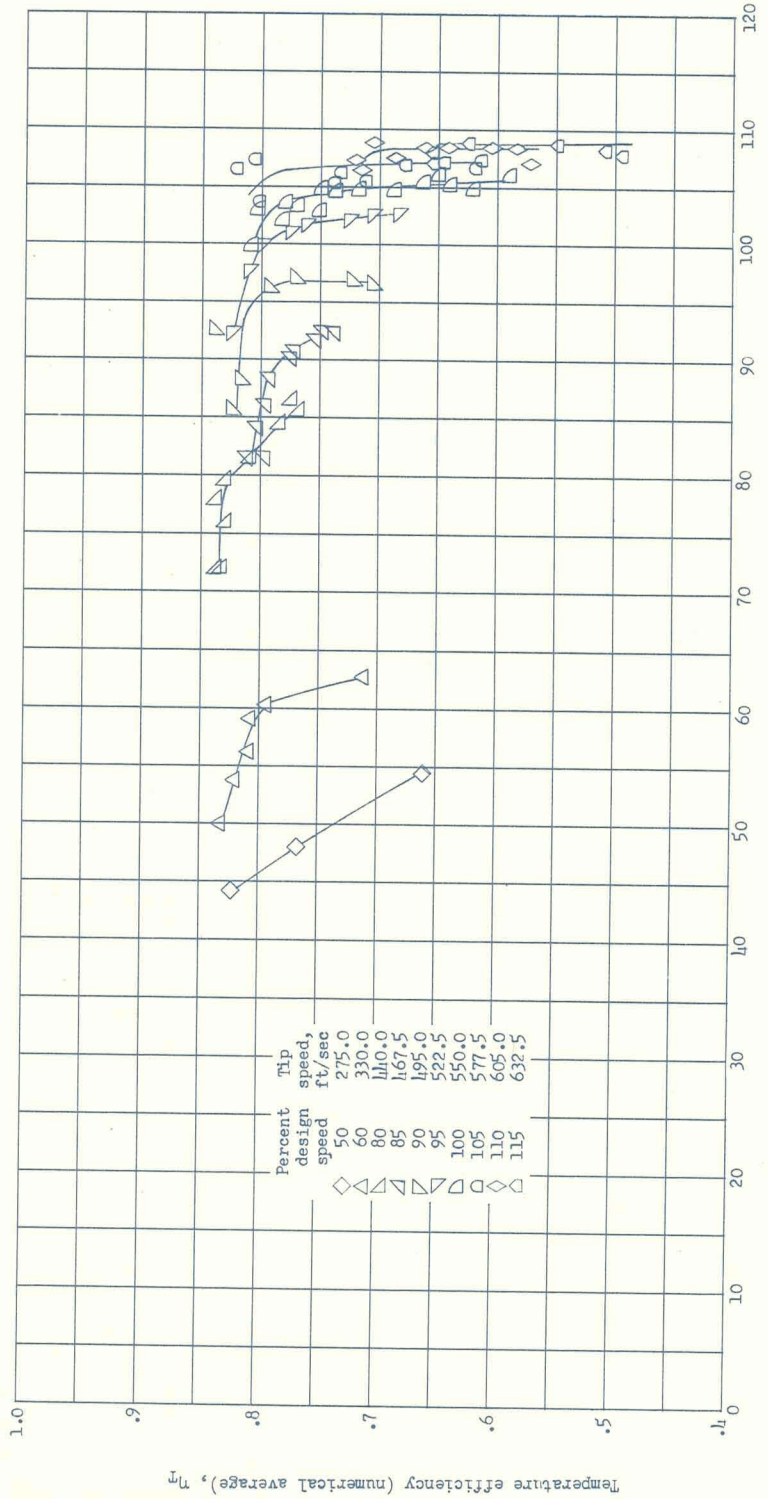

(b) Variation of temperature efficiency (numerical average) with percent of design mass flow.

Figure 15.- Continued.

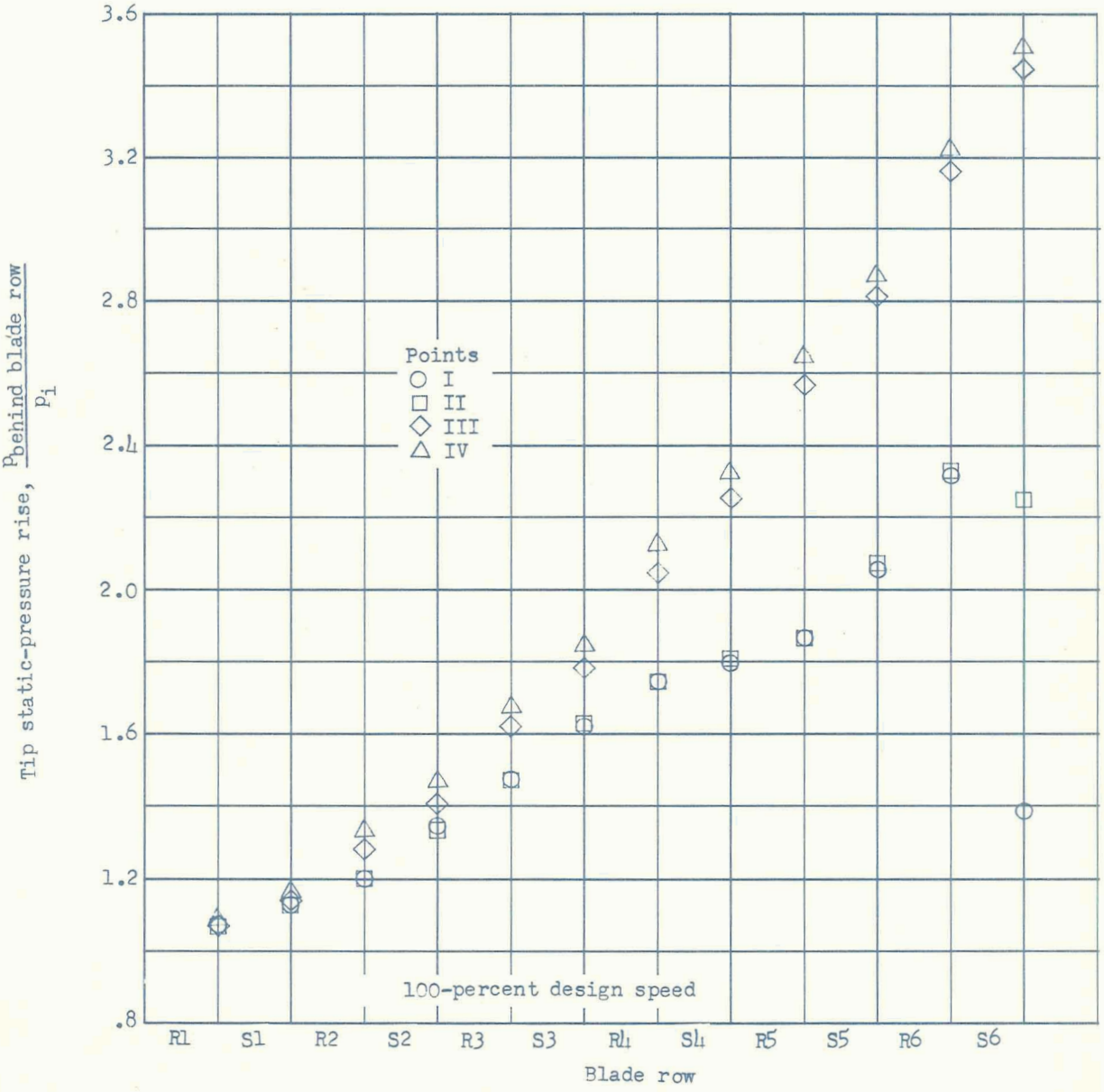

(c) Variation of tip static-pressure rise with blade row.

Figure 15.- Continued.

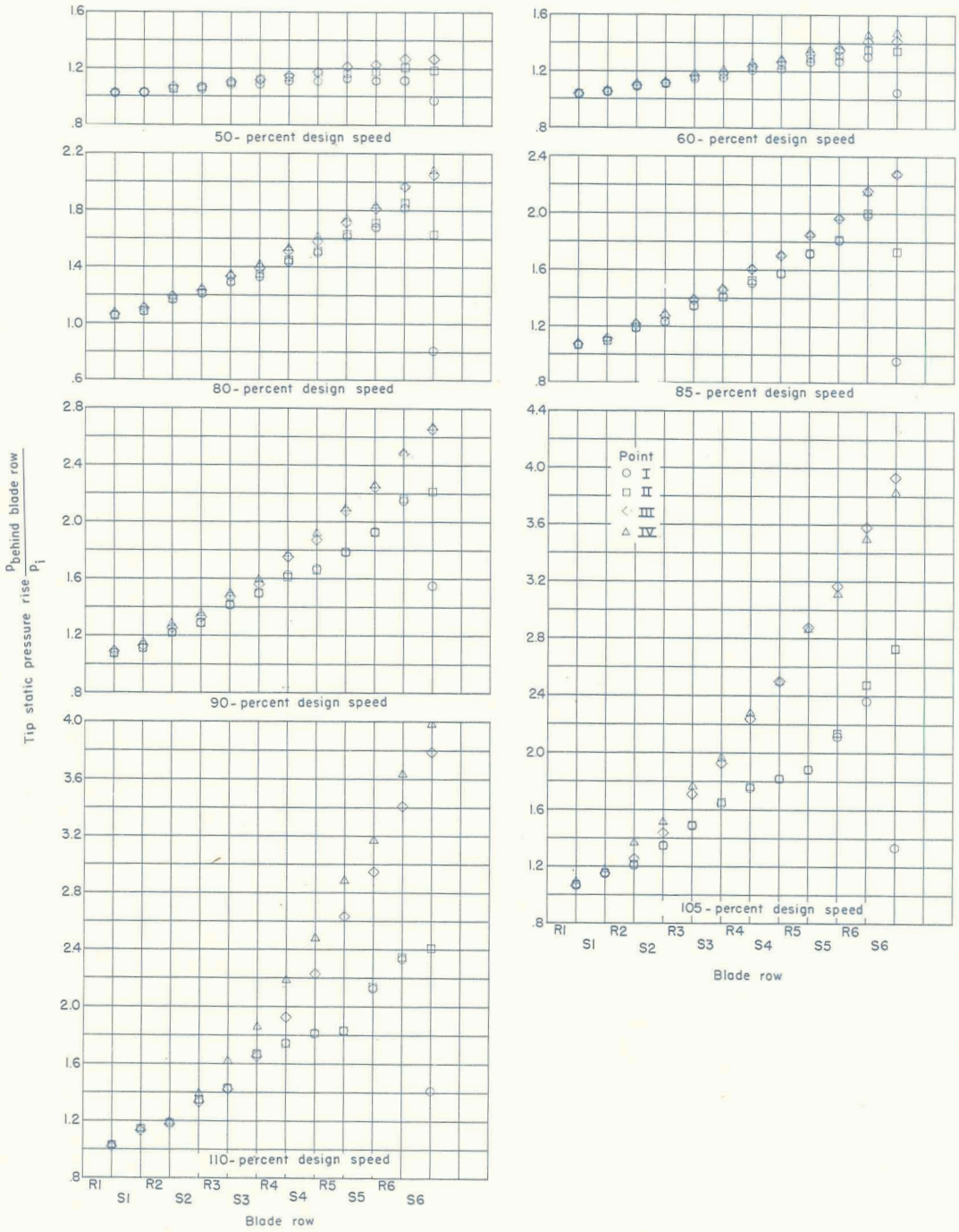

(c) Concluded.

Figure 15.- Concluded.

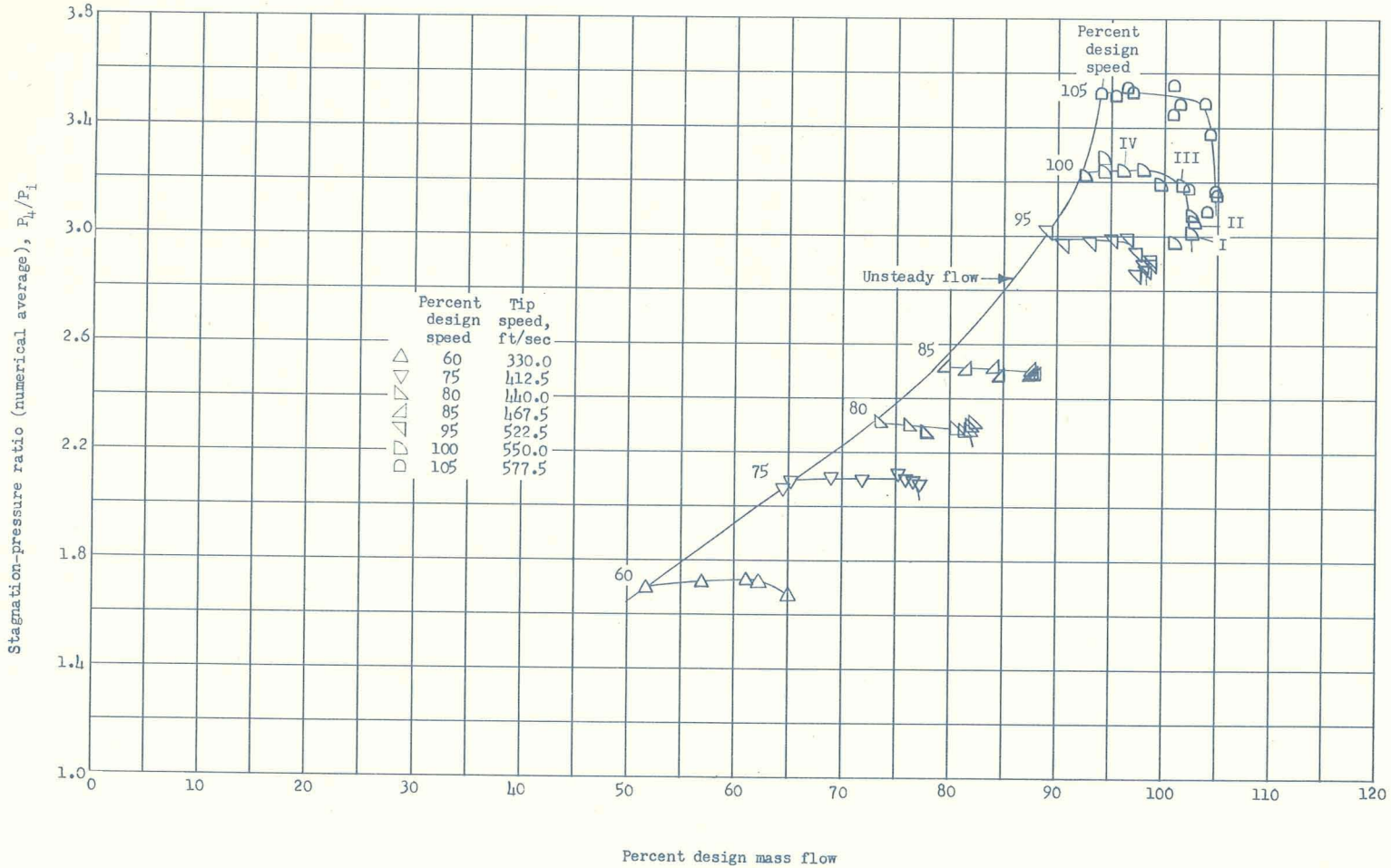

(a) Variation of stagnation-pressure ratio (numerical average) with percent of design mass flow.

Figure 16.- Overall performance of a six-stage axial-flow compressor configuration D in air.

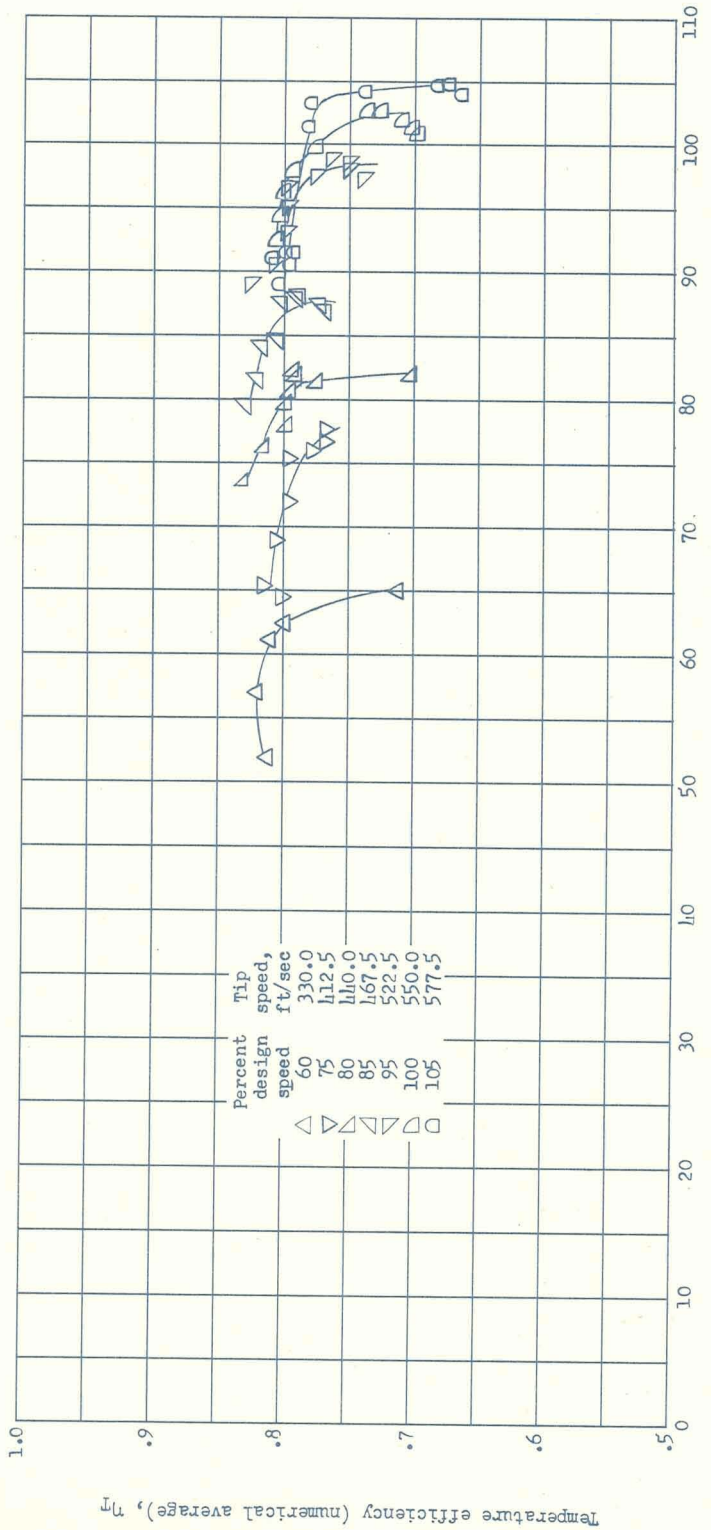

(b) Variation of temperature efficiency (numerical average) with percent of design mass flow.

Figure 16.- Continued.

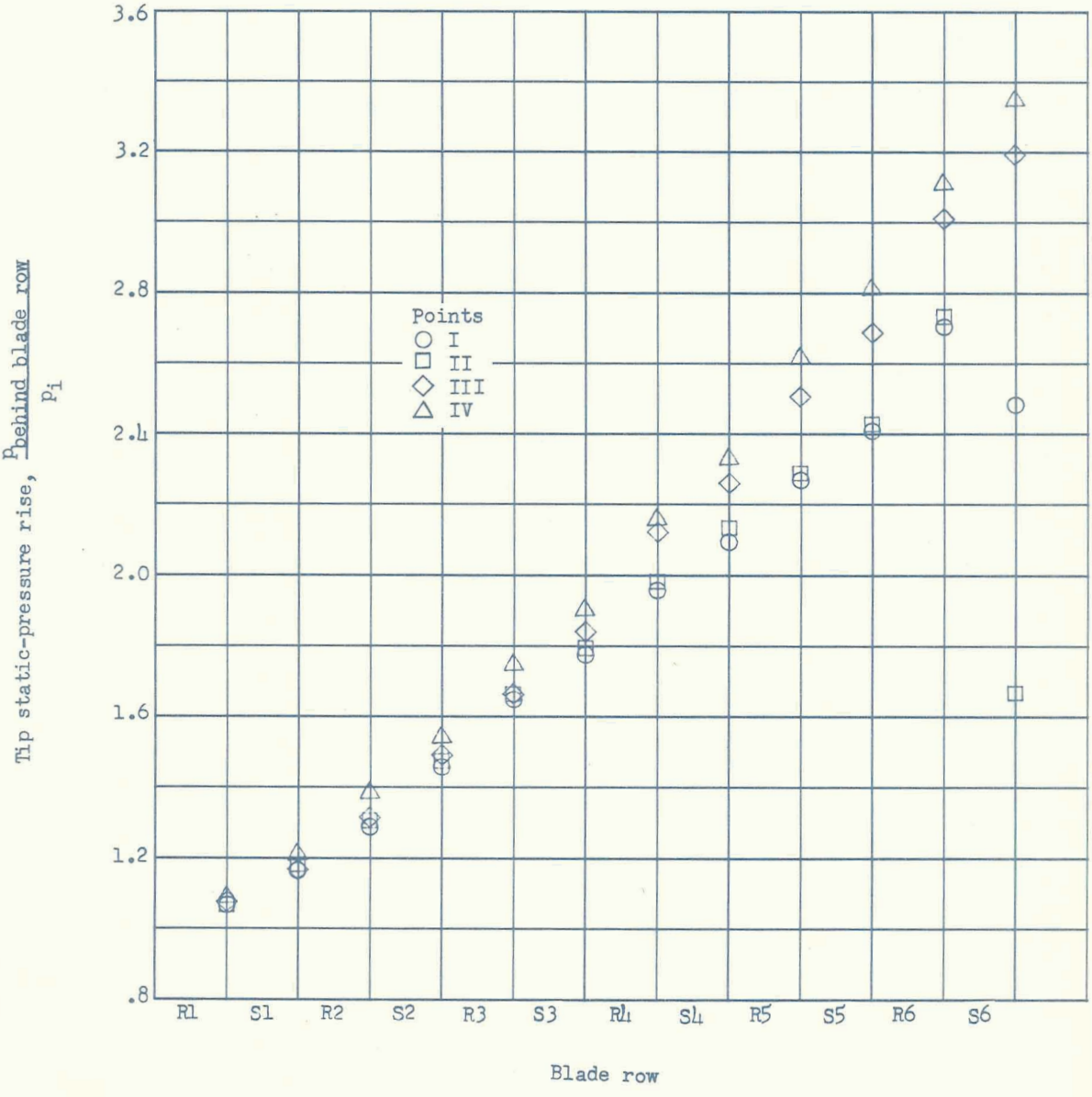

(c) Variation of tip static-pressure rise with blade row at 100-percent design speed.

Figure 16.- Concluded.

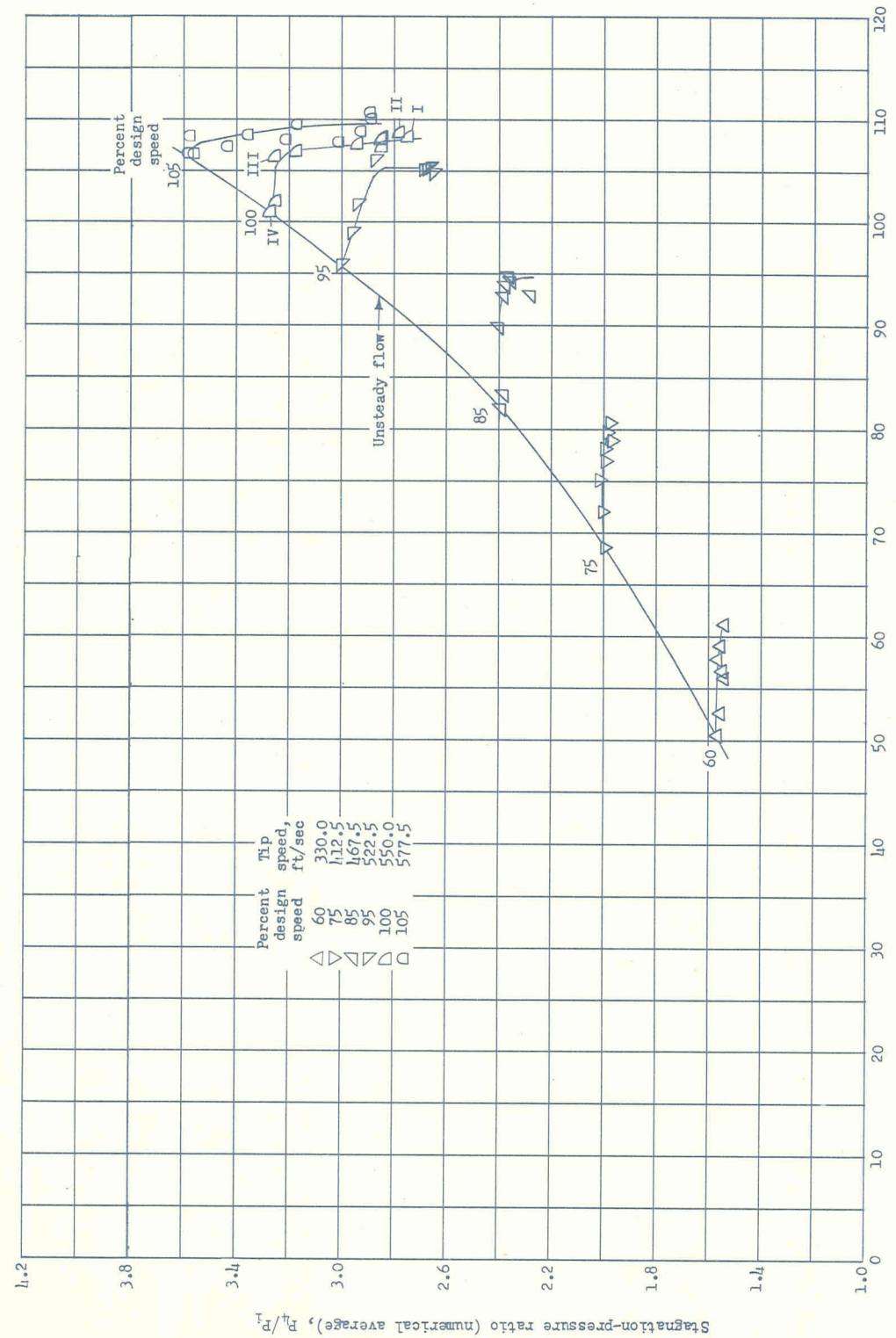

(a) Variation of stagnation-pressure ratio (numerical average) with percent of design mass flow.

Figure 17.- Overall performance of a six-stage axial-flow compressor configuration D in Freon-12.

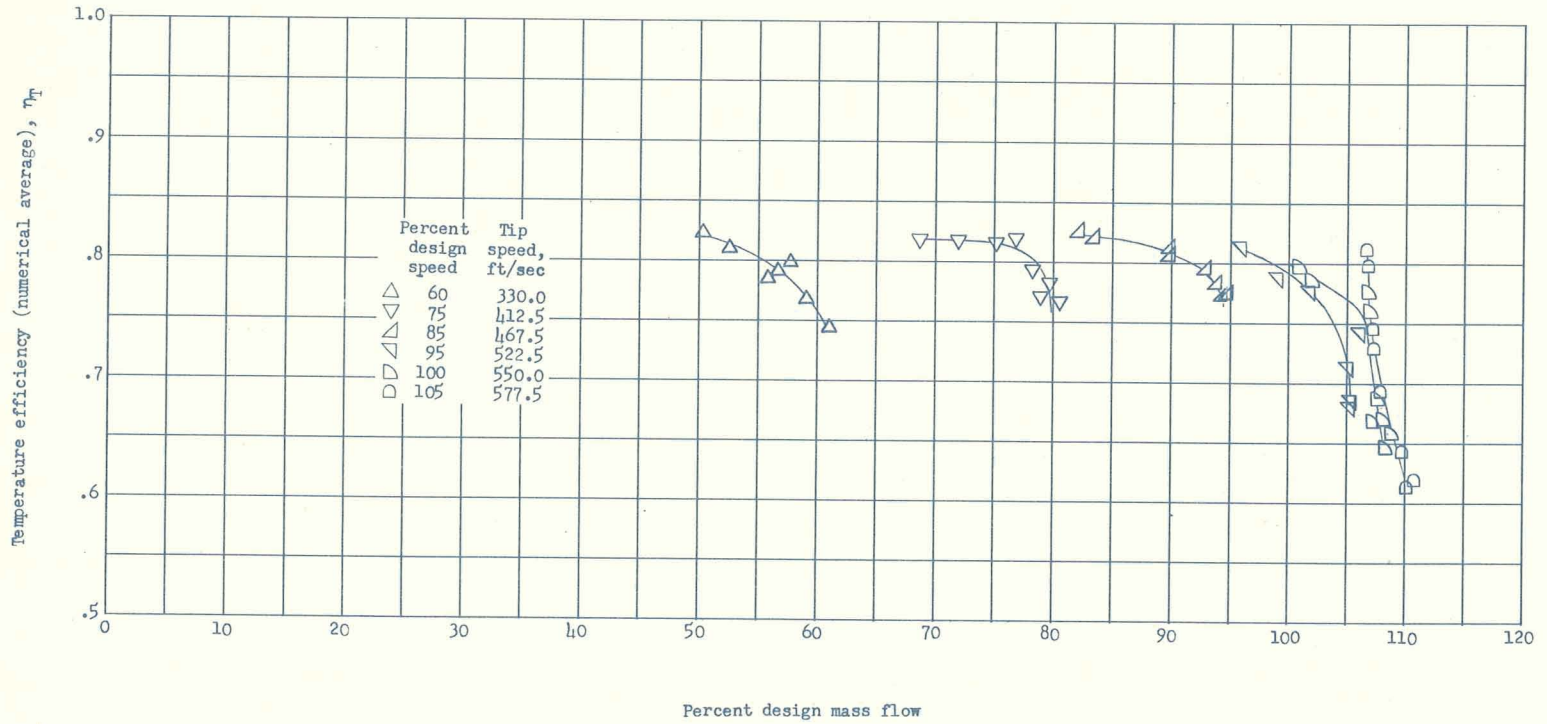

(b) Variation of temperature efficiency (numerical average) with percent of design mass flow.

Figure 17.- Continued.

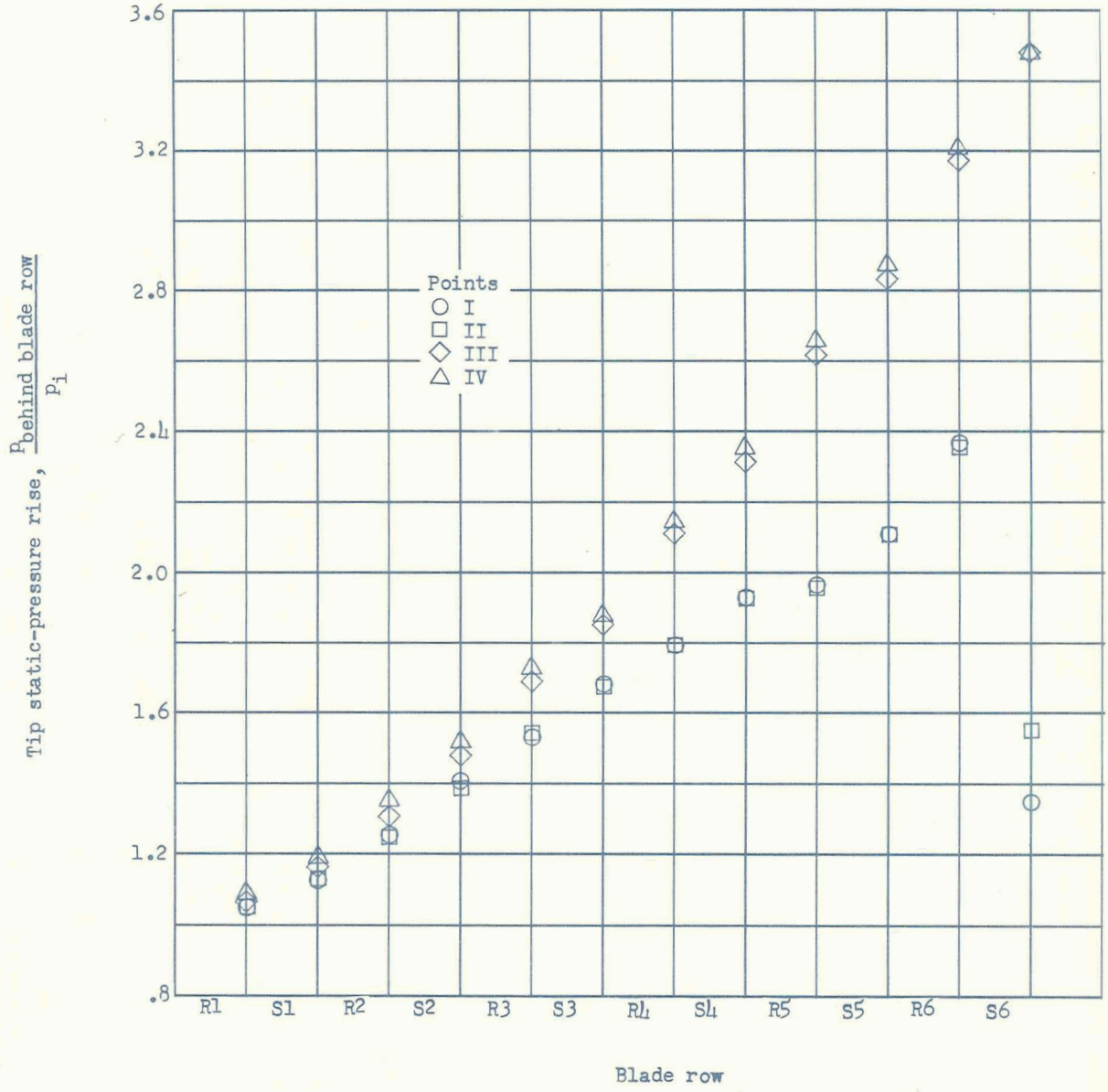

(c) Variation of tip static-pressure rise with blade row at 100-percent design speed.

Figure 17.- Concluded.

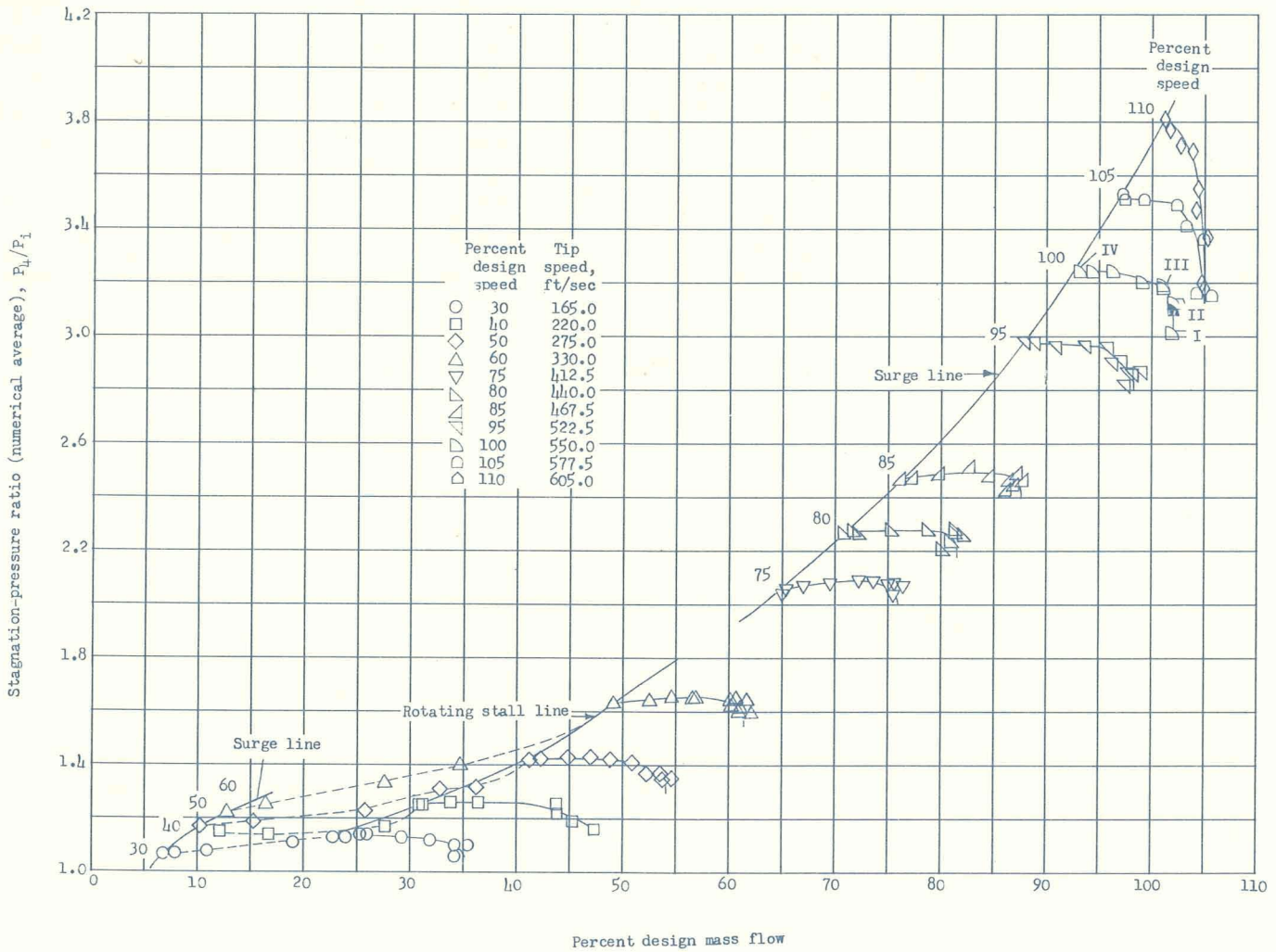

(a) Variation of stagnation-pressure ratio (numerical average) with percent of design mass flow.

Figure 18.- Overall performance of a six-stage axial-flow compressor configuration E in air.

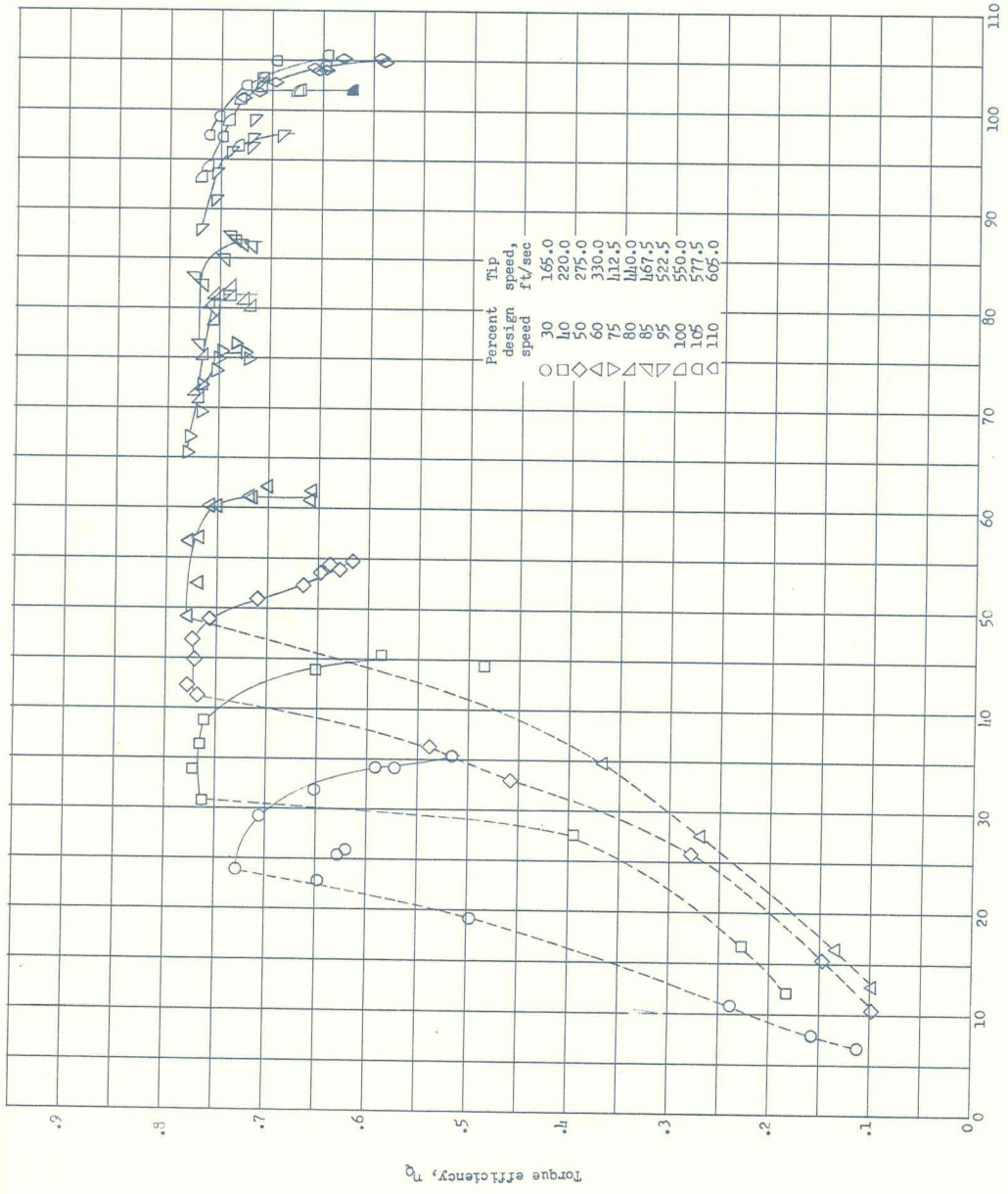

(b) Variation of torque efficiency with percent of design mass flow.

Figure 18.- Continued.

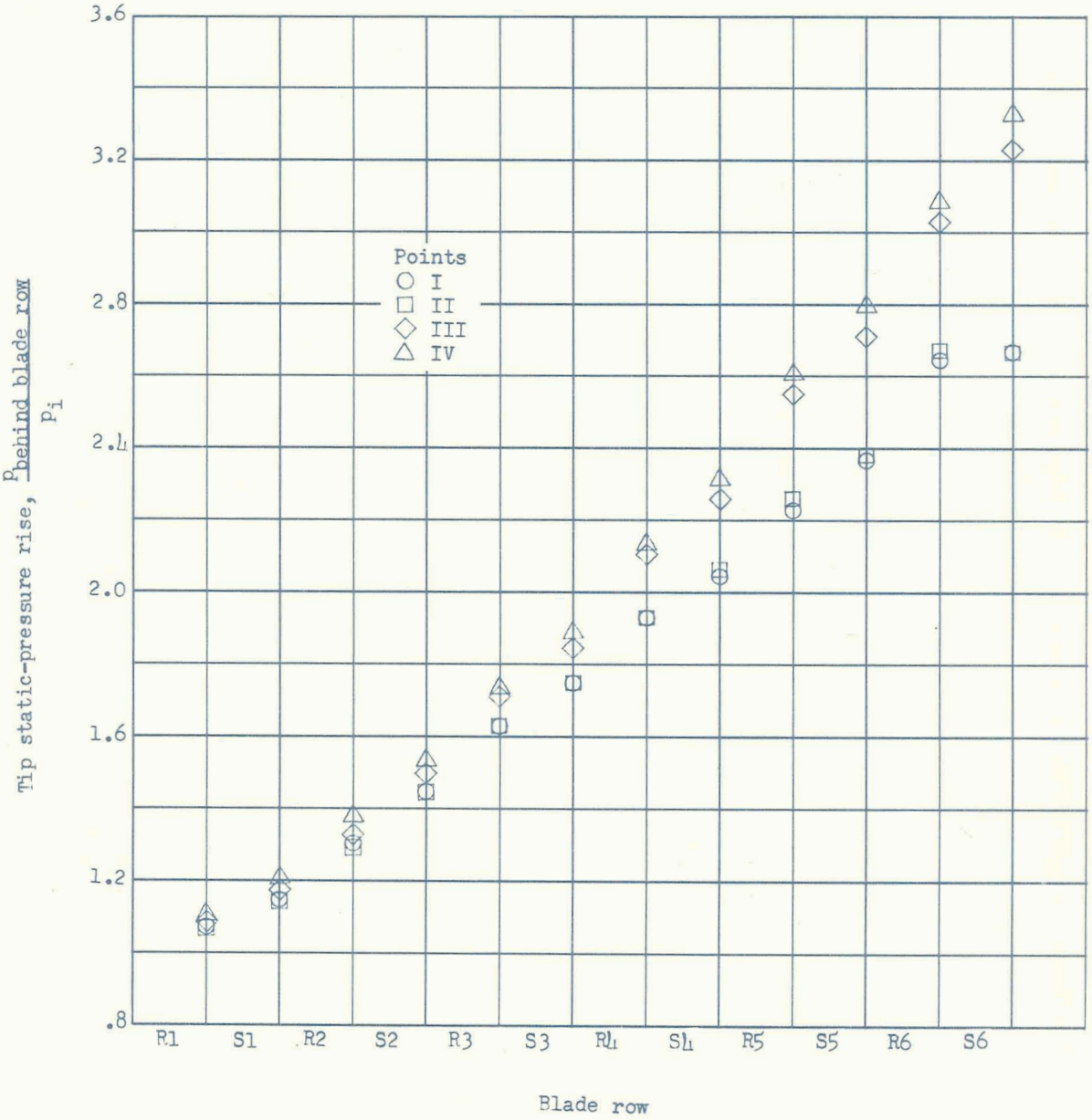

(c) Variation of tip static-pressure rise with blade row at 100-percent design speed.

Figure 18.- Concluded.

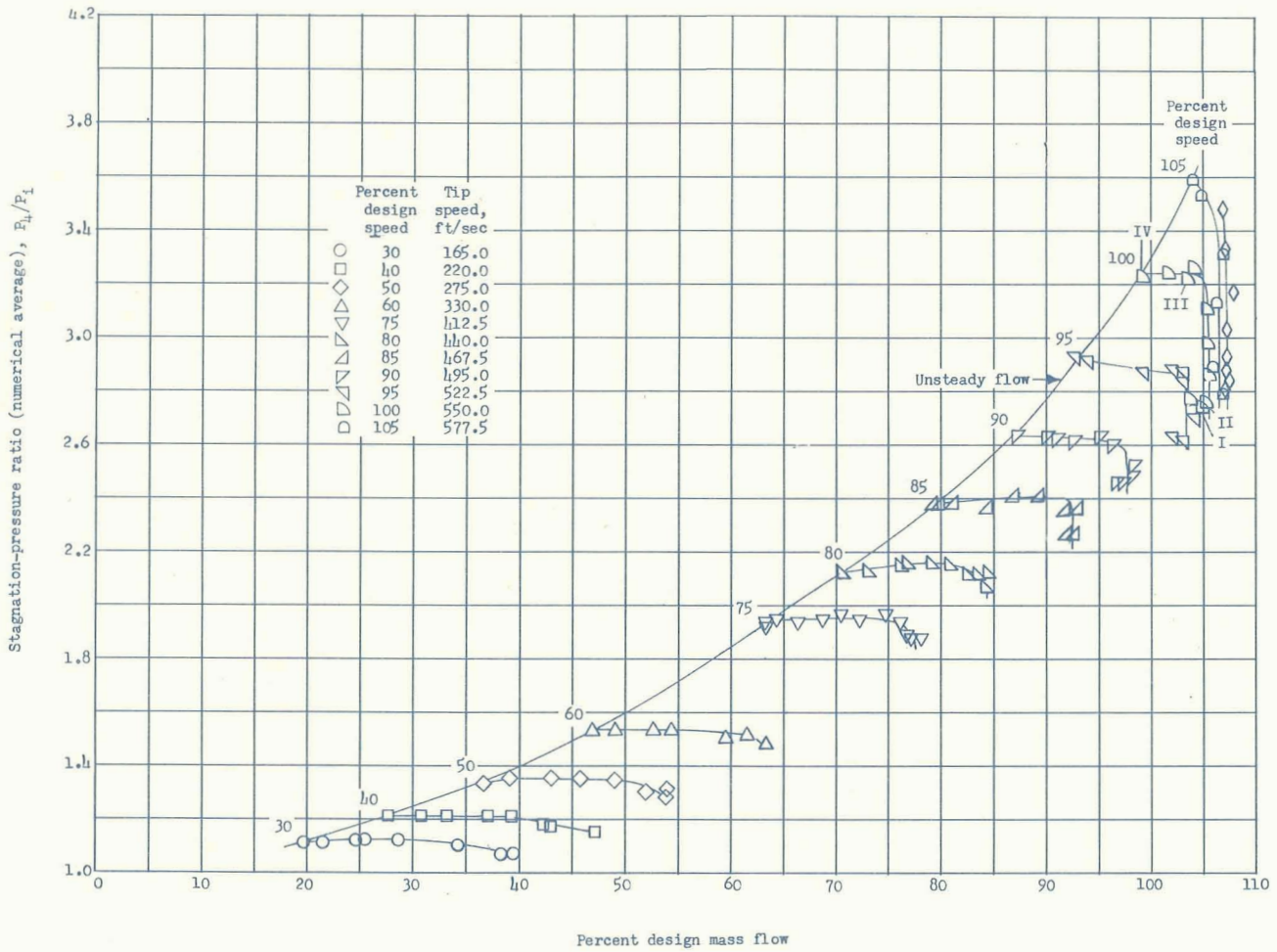

(a) Variation of stagnation-pressure ratio (numerical average) with percent of design mass flow.

Figure 19.- Overall performance of a six-stage axial-flow compressor configuration E in Freon-12.

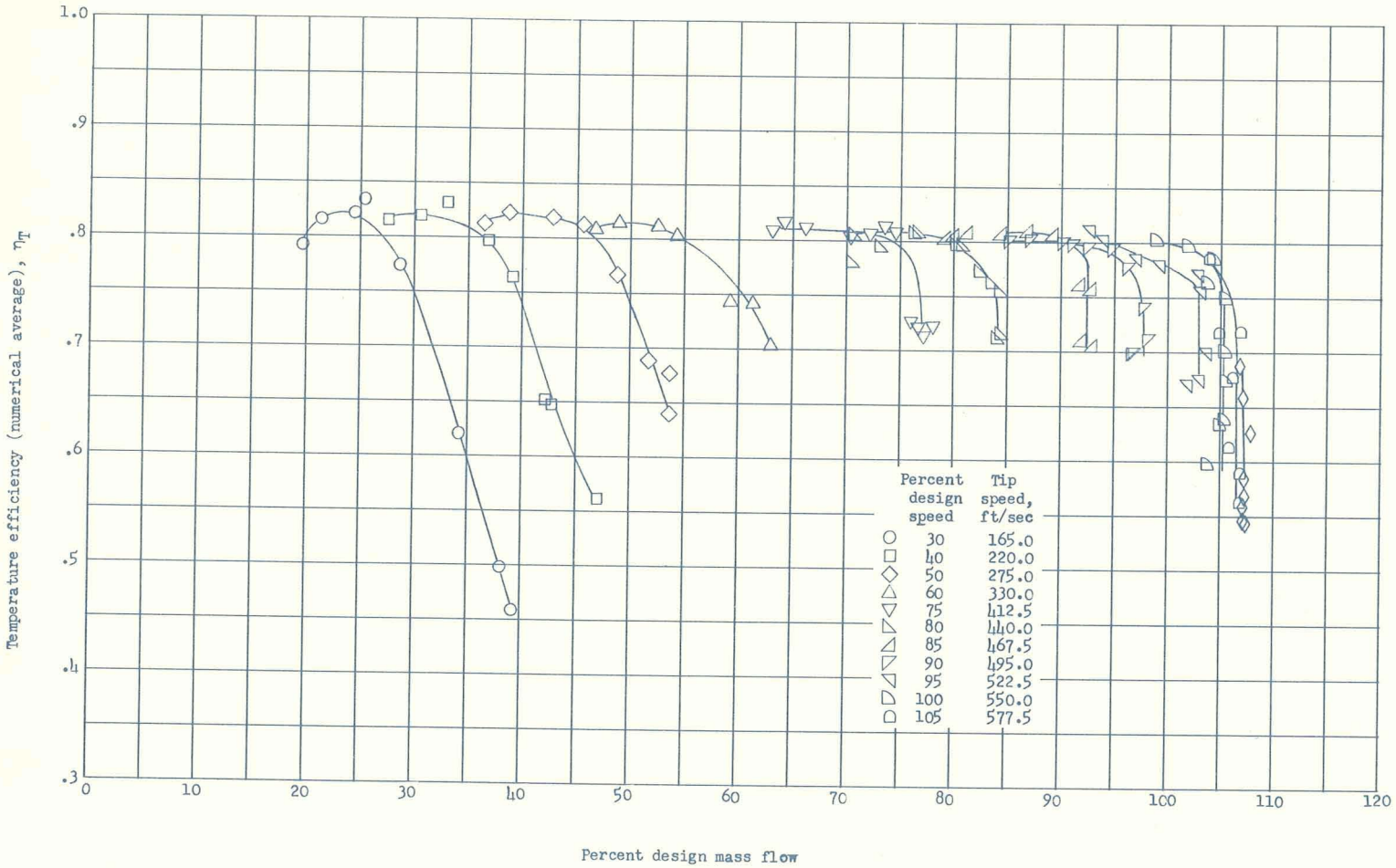

(b) Variation of temperature efficiency (numerical average) with percent of design mass flow.

Figure 19.- Continued.

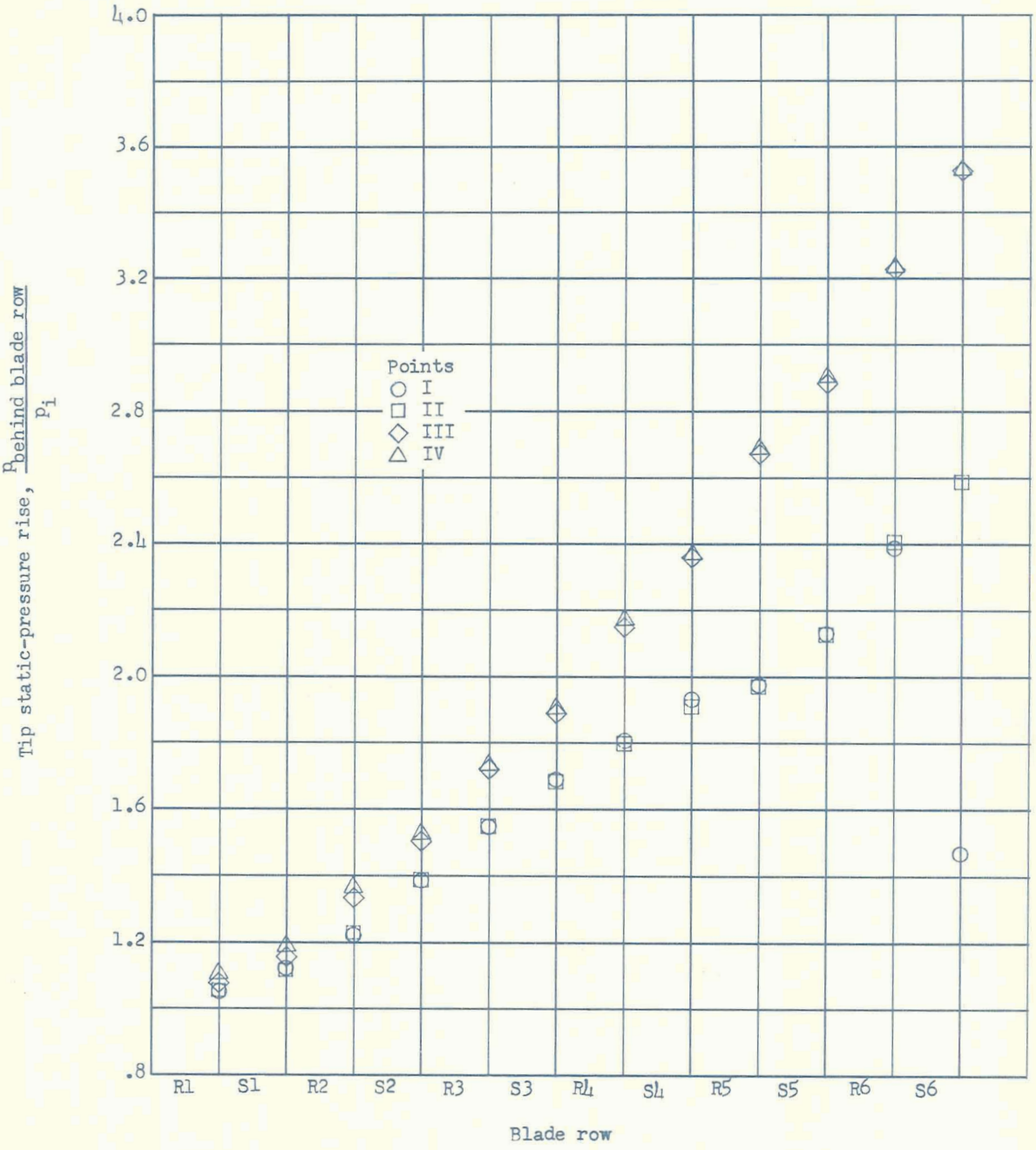

(c) Variation of tip static-pressure rise with blade row at 100-percent design speed.

Figure 19.- Concluded.